

Article

# Qualitative and Quantitative Transient Stability Assessment of Stand-Alone Hybrid Microgrids in a Cluster Environment

Kishan Veerashekar \*, Halil Askan  and Matthias Luther

Institute of Electrical Energy Systems, Friedrich-Alexander-Universität Erlangen-Nürnberg, Cauerstr. 4 (House No. 1), 91058 Erlangen, Germany; halil.askan@fau.de (H.A.); matthias.luther@fau.de (M.L.)

\* Correspondence: kishan.veerashekar@fau.de

Received: 29 January 2020; Accepted: 8 March 2020; Published: 10 March 2020



**Abstract:** Neighboring stand-alone hybrid microgrids with diesel generators (DGs) as well as grid-feeding photovoltaics (PV) and grid-forming battery storage systems (BSS) can be coupled to reduce fuel costs and emissions as well as to enhance the security of supply. In contrast to the research in control and small-signal rotor angle stability of microgrids, there is a significant lack of knowledge regarding the transient stability of off-grid hybrid microgrids in a cluster environment. Therefore, the large-signal rotor angle stability of pooled microgrids was assessed qualitatively and also quantitatively in this research work. Quantitative transient stability assessment (TSA) was carried out with the help of the—recently developed and validated—micro-hybrid method by combining time-domain simulations and transient energy function analyses. For this purpose, three realistic dynamic microgrids were modelled regarding three operating modes (island, interconnection, and cluster) as well as the conventional scenario “classical” and four hybrid scenarios (“storage”, “sun”, “sun & storage”, and “night”) regarding different instants of time on a tropical partly sunny day. It can be inferred that, coupling hybrid microgrids is feasible from the voltage, frequency, and also transient stability point of view. However, the risk of large-signal rotor angle instability in pooled microgrids is relatively higher than in islanded microgrids. Along with critical clearing times, new stability-related indicators such as system stability degree and corrected critical clearing times should be taken into account in the planning phase and in the operation of microgrids. In principle, a general conclusion concerning the best operating mode and scenario of the investigated microgrids cannot be drawn. TSA of pooled hybrid microgrids should be performed—on a regular basis especially in the grid operation—for different loading conditions, tie-line power flows, topologies, operating modes, and scenarios.

**Keywords:** critical clearing times; diesel generators; grid-feeding photovoltaics; grid-forming battery storage systems; stand-alone hybrid microgrids; system stability degree; the micro-hybrid method; transient stability assessment

## 1. Introduction

Autonomous hybrid microgrids with diesel and/or biogas engine-driven synchronous generators as well as grid-feeding photovoltaics (PV) and grid-forming battery storage systems (BSS) are being widely installed in developing and underdeveloped countries [1–4]. By coupling spatially close stand-alone hybrid microgrids, it is possible to curtail fuel costs and emissions, and to enhance the security of supply [5,6].

Such clustered microgrids should be investigated from the system stability point of view. Voltage stability analysis has been carried out in an interconnected AC-DC microgrid under fault conditions [7].

In [8], clustering two microgrids comprising a synchronous generator and two inverter-based systems was studied with respect to blackouts. Small-signal stability of AC and DC microgrids in a cluster environment was analyzed in [9–13]. Ref [9] deals with the implementation of a hierarchical control scheme for DC microgrid clusters. Eigenvalue analysis was performed from the control point of view in [10] considering two interconnected DC microgrids. On the other hand, [11] dealt with the small-signal stability assessment of clustered AC microgrids comprising inverter-based distribution generation units. Identification of critical microgrid clusters was carried out using a stability indicator, i.e., stability margin based on the active power droop of the inverters. In [12], multiple inverter-based microgrid clusters were analyzed from the small-signal stability analysis and the dynamic behavior point of view. In addition to the eigenvalue analysis of a cluster of four identical microgrids, optimal parametrization of controllers was performed—using the particle swarm optimization—to improve the system stability [13]. However, there is a significant lack of research in the qualitative and especially in the quantitative transient stability assessment (TSA) of clustered microgrids.

Large-signal rotor angle stability of clustered microgrids with synchronous generators should be analyzed both in the short-term and long-term planning phase as well as in the operation [14,15]. A detailed dynamic microgrid modelling and knowledge of system response in case of three-phase faults—especially critical faults—are essential for an effective qualitative TSA, which is performed with the help of time-domain simulations (TDS) [14,16]. The qualitative TSA of microgrids comprising diesel generators (DGs) and PV, acting as current sources as well as static loads (SL) was investigated taking different microgrid models in [17] and [18].

On the other hand, online and/or offline quantitative TSA using hybrid methods—combining TDS and transient energy function (TEF) analyses—allows determining the dynamic (operational) limits in microgrids [15]. In [19], the new hybrid method was proposed and applied in an one-machine infinite bus microgrid and two machine microgrid taking classical and detailed models of DGs with and without controllers into account. Furthermore, the other five hybrid methods have been briefly discussed in [19].

Due to a discrepancy in the profiles of kinetic energy (KE) and potential energy (PE), the new hybrid technique was improved by adjusting the TEF for microgrids [20]. In [20] the micro-hybrid method (the improved new hybrid method) was verified and applied in a stand-alone microgrid with three DGs. Furthermore, quantitative TSA was performed in off-grid DG-based microgrids—without inverter-based systems such as PV and BSS as well as dynamic loads—for different coupling degrees by considering a short-circuit location [20].

Regarding microgrids in a cluster environment, there is a need to analyze the transient stability of off-grid hybrid microgrids, comprising synchronous generators and inverter-based PV and BSS, both qualitatively and quantitatively. The dynamic performance of stand-alone hybrid microgrids with DGs, grid-feeding PV, grid-forming BSS, and static and dynamic loads, under three-phase short-circuit conditions has not been investigated in-depth so far. This calls for a detailed dynamic system modelling. From the feasibility and system stability point of view, the influence of different degrees of clustering should be investigated. The quantitative TSA performed using the (recently proposed and verified) new hybrid method [19] and the micro-hybrid method [20], in microgrids with only DGs, can be now applied in hybrid microgrids. Further, no research has yet been performed in off-grid microgrids, taking system's and critical machine's critical energy (KE/PE) into account. Hence, in the framework of this research, the following tasks were executed with the help of software DIGSILENT® (Gomaringen, Germany) PowerFactory™ (v2017.0.2), and MathWorks® (Natick, USA) MATLAB™ (vR2016b):

- Detailed dynamic modelling of classical and hybrid microgrids—representing four hybrid scenarios with respect to different points in time on a summer day—comprising DGs, grid-feeding PV, grid-forming BSS, as well as static and dynamic loads in a cluster environment.
- Comparison of critical clearing time (CCT) profiles of the microgrids with respect to the four hybrid scenarios and the classical scenario (with DGs only) as well as three operating modes, namely island, interconnection, and cluster mode.

- Qualitative stability assessment by comparing the behavior of the four hybrid microgrids (i.e., hybrid scenarios in cluster mode) with that of the classical microgrid for a three-phase short-circuit location.
- Qualitative investigation of the impact of different degrees of coupling (i.e., operating modes) of microgrids on the system stability.
- Quantitative TSA using the micro-hybrid method in the scenarios and operating modes by investigating the system stability degree with respect to different clearing times for the same fault location.
- Quantitative analysis of the critical energy and of the effect of the fault location on the critical energy in the cluster mode.

In this research paper fundamentals will not be given in a separate chapter, since the relevant basics have already been presented in recently published journal articles [19,20]. Hence, the focus will be laid on methodology and results. The rest of the paper is structured as follows: In Chapter 2, the methodological approach will be explained in detail. The modelled microgrids, the scenarios and the operating modes together with the dimensioning of the controllers in PV and BSS will be described. The last subchapter deals with the approach with respect to the qualitative and quantitative TSA. Chapter 3 describes the simulation results and the corresponding discussion. The first part of this chapter focuses on the results of the qualitative TSA, whereas the second part deals with the quantitative TSA. A detailed summary of the research work along with the key findings, as well as an outlook, will be given in Chapter 4.

## 2. Methodology

### 2.1. System Modelling

The model of the three coupled or pooled rural microgrids comprising DGs and static loads has been presented in previous papers [17,20,21]. The topology of the stand-alone microgrids was slightly extended in this research work (see Figure 1) in order to connect grid-feeding PV, grid-forming BSS, as well as dynamic loads. The installed capacity of the clustered microgrid is ca. 950 kW. The ratio of the static to dynamic loads was exemplarily selected to be 0.8:0.2. The load was assumed to be high, such that the actual load is equal to 80% of the nominal power demand. The modelling and RMS-simulations of these microgrids were performed in software DIgSILENT® PowerFactory™.

The dimensioning of the DGs, PV, and BSS as well as the powers was performed according to following criterion:

- High mechanical (engine) loading of DGs (70%–80%)
- High PV feed-in (75%–85% of the nominal real power)
- High consumption/feed-in of BSS (60%–90% of the nominal real power)
- Allowable maximum and minimum voltage and frequency values according to the international norm ISO 8528-5 in the steady-state and sudden load change.

The details of the 5th order modelling of diesel engine-driven synchronous generators [22] from Stamford® [23] along with speed governor and voltage controller have been given in [17,20,21]. The nominal real power of DGs is between 24 and 112 kW (power factor of 0.8)—apparent power between 30 and 140 kVA. In total 12 DGs (4 DGs per microgrid) were installed in the cluster mode, such that 6 DGs were assumed to be reserve DGs. They were connected or disconnected depending on the point in time (scenario), whereas the other 6 DGs were operated continuously.

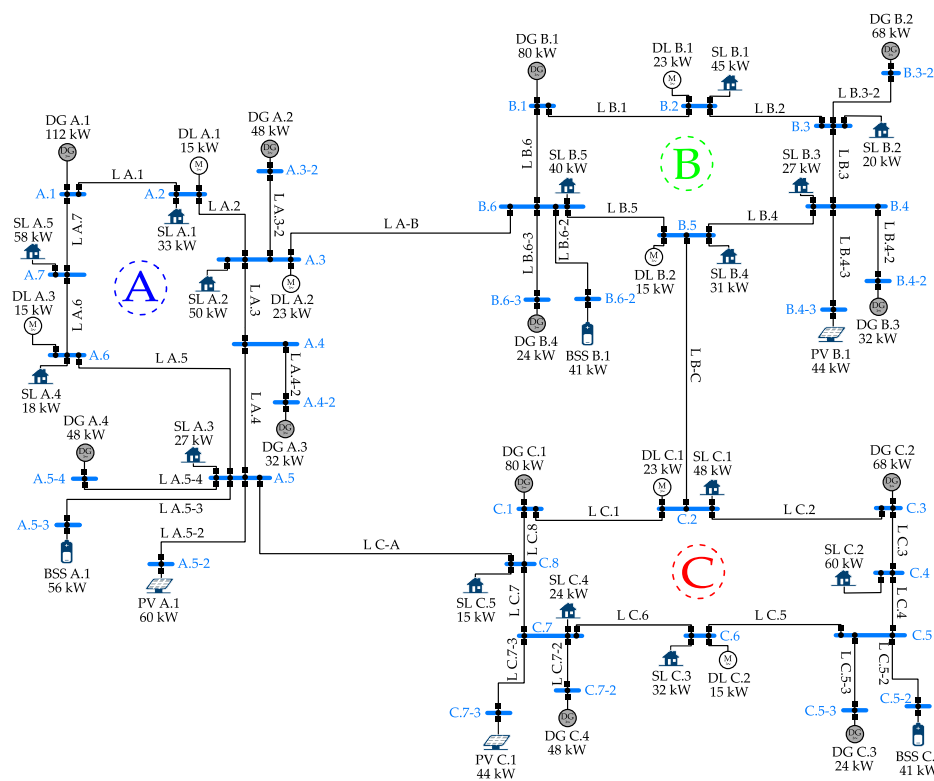


**Figure 1.** Topology of the investigated microgrids in the cluster mode with diesel generators (DGs), photovoltaics (PV), battery storage systems (BSS), and static and dynamic loads.

PV systems were modelled considering the DC-side. The dimensioning of the main components of PV systems—PV generator, DC-link capacitor, and L filter—has been explained in [17]. In this research work, each microgrid comprises one PV system. The nominal active power of PV A.1 is 60 kW and PV B.1 and C.1 is 44 kW, with a constant power factor of 0.95 (cap.). Each PV generator is made up of 28 modules in series and 6–9 modules in parallel—belonging to Sharp® NQ-R258H [24]. The employed inverters are Sunny TP 60 and Sunny TP Core1 [25,26]. The investigated day was assumed to be a partly sunny day in a tropical country, where the solar irradiance and the PV module temperature is equal to  $1000 \text{ W/m}^2$  and  $60 \text{ }^\circ\text{C}$ , respectively. On the other hand, the DC-side of BSS was not considered in the framework of this research work. The inverter of BSS was connected to an ideal DC voltage source. The nominal power of BSS A.1 and BSS B.1 and C.1 is 56 kW and 41 kW, respectively, with a power factor of 0.95 (cap.). The dimensioning of the controllers used in the grid-feeding PV systems and grid-forming BSS will be described in Section 2.3.

In contrast to transmission systems, modelling microgrids' loads exclusively as SL does not lead to convincing results. [27] Off-grid microgrids are usually relatively smaller in size and lack historical measurement data. Hence, dynamic loads were modelled directly in the studied microgrids instead of considering composite dynamic load models [28,29]. In this research work—the most widely employed dynamic loads—double-cage induction motors were taken into account for small-scale agricultural activities, namely water pumps and sugarcane crushers [30,31]. On the other hand, the majority (80%) of the loads were modelled as static and constant impedance loads, which are voltage dependent and frequency independent. According to ISO 8528-5, the modelled static loads belong to class G2 [32,33]. Each microgrid has a total nominal power of loads of roughly 200 kW.

## 2.2. Overview of Scenarios and Operating Modes

In the framework of this research, five scenarios and three operating modes were analyzed. Depending on the point in time during the partly sunny day, four scenarios were considered as

hybrid. The classical scenario was also analyzed to compare the hybrid microgrids with the traditional microgrids comprising DGs only. Table 1 lists the investigated scenarios, where the BSS act as loads and generating units in scenario “storage” and “sun & storage”, respectively. The load demand remains the same in all the scenarios, i.e., 80% of the nominal power. Further, the solar irradiance and the PV module temperature were assumed to be constant in the corresponding hybrid scenarios. BSS were disconnected in scenario “sun”, whereas PV systems were considered to be inactive in scenario “night”.

**Table 1.** Overview of the five investigated scenarios.

Scenario	Name (Time of Day)	Short Form	Active Equipment
Classical	Classical (-)	Cl	DGs
Hybrid	Storage (12 pm)	St	DGs + PV + BSS (load)
	Sun (2 pm)	Su	DGs + PV
	Sun & Storage (3 pm)	S&S	DGs + PV + BSS (generation)
	Night (8 pm)	Ni	DGs + BSS (generation)

The total installed capacity of DGs, PV, and BSS in each hybrid microgrid is listed in Table 2. The nominal active power of the clustered microgrid lies around 950 kW, whereas the total load demand is about 650 kW. In the classical scenario with DGs only, the installed capacity of the DGs remains unchanged—i.e., equal to 665 kW, which is slightly higher than that of loads. The ratio of the total nominal active power of DGs, PV, and BSS lies around 70:15:15, independent of the operating mode.

**Table 2.** Nominal active power (in kW) of DGs, PV, BSS, and loads in the hybrid microgrids.

	Generation				Load	DG:PV:BSS
	DG	PV	BSS	Total		
Microgrid A	240	60	56	355	239	67:17:16
Microgrid B	204	44	41	289	201	71:15:14
Microgrid C	220	44	41	305	217	72:15:13
Cluster	<b>664</b>	<b>148</b>	<b>138</b>	<b>949</b>	<b>656</b>	<b>70:16:14</b>

Depending on the time of day (scenario) and degree of coupling (operating mode), reserve DGs were activated or deactivated, such that the engine loading lies between 70% and 80%—see Section 2.1. According to Table 3, the minimum number of active DGs is equal to 2 (“sun & storage” in the island mode), while the maximum number of operating DGs is 12 (“classical” and “storage” in the cluster mode). In this research work, only microgrid C is studied in the islanded (ISD) mode, whereas the coupling of microgrid A and C is investigated in the interconnected (INT) mode. Microgrid A, B, and C are connected with each other in the form of a ring in the clustered (CLS) mode.

**Table 3.** Overview of the number of active DGs according to scenarios and operating modes.

	Classical	Storage	Sun	Sun & Storage	Night
<b>Island</b>	4	4	3	2	3
<b>Interconnection</b>	8	8	6	4	6
<b>Cluster</b>	12	12	8	6	8

The percentage share of the actual active power of DGs, PV, and BSS in each operating mode is illustrated in Figure 2. Since BSS act as loads in “storage” unlike in “sun & storage”, BSS are not shown in the graphs. The highest amount of inverter-based systems is observed in “sun & storage”. It should be noted that, the power exchange between the microgrids is negligible in both the interconnected and clustered mode. However, the effect of pooling microgrids with significant power exchange on the system stability can be analyzed in the future research work.

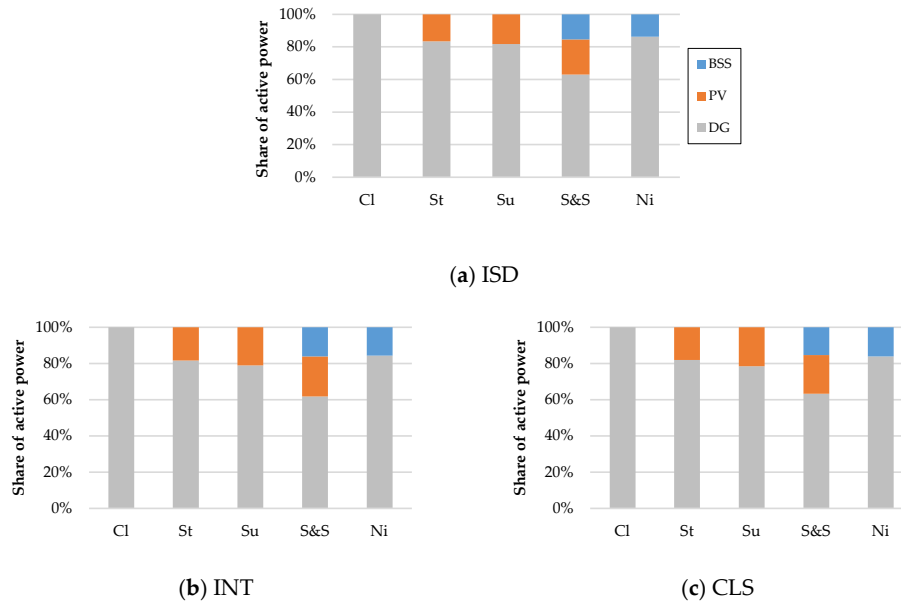


Figure 2. Percentage of actual real power of DGs, PV, and BSS in the scenarios: island (a), interconnection (b), and cluster (c) mode.

### 2.3. Dimensioning of Controllers in Photovoltaics and Battery Storage Systems

#### 2.3.1. Photovoltaics

Figure 3 depicts the block diagram of grid-feeding PV systems with respective controllers. The inner and outer control loop corresponds to the current and DC voltage controller, respectively. The fundamentals of this block diagram have been given in [17,34,35]. In this section, the dimensioning of the PI controller in the current and DC voltage control block will be discussed.

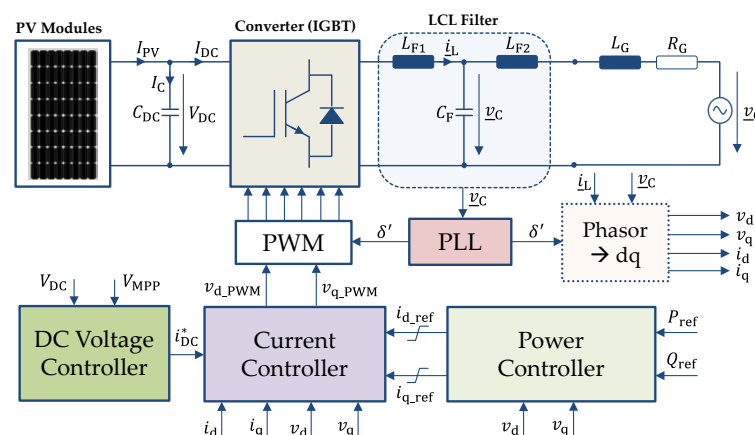


Figure 3. Block diagram of grid-feeding photovoltaics with corresponding controllers, according to [35,36].

### Current Controller

The block diagram of the current control loop comprises a PI controller and a controlled plant, which is made up of three first-order delay blocks [35]—cf. Figure 4. In order to reduce the complexity in representing the transfer function of the plant, an L filter was taken into consideration [35]. In principle, modulus optimum can be employed to dimension the parameters of the PI controller ( $K_{pc}$  and  $T_{ic}$ ), since there is no integrator block in the controlled plant [37].

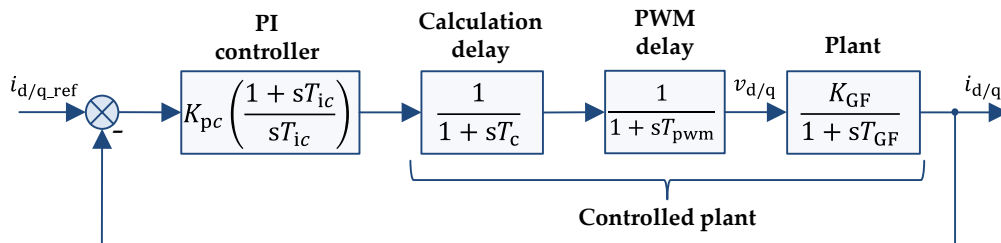


Figure 4. Block diagram of the inner control loop in PV, according to [35].

However, due to the fact that  $T_{GF} > 4T_{\alpha}$ , symmetrical optimum was used for dimensioning  $K_{pc}$  and  $T_{ic}$  [37].  $T_{GF} = L_{GF}/R_{GF}$ , where the numerator and denominator are the sum of equivalent short-circuit inductance and resistance at the point of common coupling as well as relatively smaller inductance and resistance of the L filter, respectively.  $T_{\alpha}$  describes the summation of the calculation delay  $T_c$  and PWM delay  $T_{pwm}$  (set integration time-step in the RMS-Simulations) [35].

The corresponding formula of  $K_{pc}$  and  $T_{ic}$  is shown in Equation (1), where  $a$  represents the variation factor [37]. According to the Bode magnitude and phase plot based on the open-loop transfer function as well as the step response of the closed-loop transfer function for  $a$  equal to 5, the control system was assessed to be stable.

$$\begin{aligned} K_{pc} &= \frac{T_{GF}R_{GF}}{aT_{\alpha}} \\ T_{ic} &= a^2T_{\alpha} \end{aligned} \tag{1}$$

Table 4 lists the PI controller parameter values of the three PV systems in the respective microgrids with regard to the three operating modes in scenario “storage”. The values corresponding to the other scenarios will not be shown. However, the calculation methodology is identical with that of scenario “storage”.

Table 4. Values of  $K_{pc}$  and  $T_{ic}$  in the current controller of PV of scenario “storage” with respect to the operating modes.

	PV A.1		PV B.1		PV C.1	
	$K_{pc}$	$T_{ic}$	$K_{pc}$	$T_{ic}$	$K_{pc}$	$T_{ic}$
<b>Island</b>	-	-	-	-	0.21	0.004
<b>Interconnection</b>	0.14	0.004	-	-	0.15	0.004
<b>Cluster</b>	0.12	0.004	0.14	0.004	0.14	0.004

### DC Voltage Controller

Figure 5 illustrates the block diagram of the outer control loop, which comprises a PI controller and a controlled plant. The latter consists of a calculation delay, inner (current) control loop, gain, and plant. The plant is an integrator block due to the DC-link capacitance. Hence, symmetrical optimum was employed for dimensioning the parameters of the PI controller  $K_{pv,DC}$  and  $T_{iv,DC}$  [37,38].

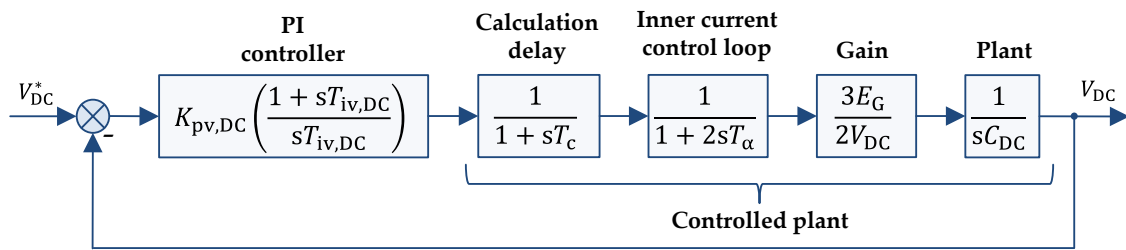


Figure 5. Block diagram of the outer control loop in PV, according to [38].

The corresponding formula of  $K_{pv,DC}$  and  $T_{iv,DC}$  is shown in Equation (2).  $C_{DC}$  and  $V_{DC}$  are the DC-link capacitance and its voltage, respectively.  $E_G$  represents the peak value of the line-ground voltage, whereas  $T_\beta$  is the summation of the time delays. [37,38]

$$\begin{aligned} K_{pv,DC} &= \frac{2C_{DC}V_{DC}}{3aE_GT_\beta} \\ T_{iv,DC} &= a^2T_\beta \end{aligned} \tag{2}$$

For  $a$  equal to 2.4 the control system was analyzed to be stable based on the Bode magnitude and phase plot as well as the step response. However, the resulting values of  $K_{pv,DC}$  and  $T_{iv,DC}$  lead to unacceptable oscillations in the investigated microgrids. The calculated values of  $K_{pv,DC}$  and  $T_{iv,DC}$  were therefore exemplarily divided and multiplied by a factor of 15 and 1000, respectively. The resulting grid simulations (without any fault or disturbance) were acceptable and plausible. The values of  $K_{pv,DC}$  and  $T_{iv,DC}$  of the PV systems for scenario “storage” with respect to the different operating modes are listed in Table 5.

Table 5. Values of  $K_{pv,DC}$  and  $T_{iv,DC}$  in the DC voltage controller of PV of scenario “storage” with respect to the operating modes.

	PV A.1		PV B.1		PV C.1	
	$K_{pv,DC}$	$T_{iv,DC}$	$K_{pv,DC}$	$T_{iv,DC}$	$K_{pv,DC}$	$T_{iv,DC}$
Island	-	-	-	-	1.14	2.0
Interconnection	1.27	2.0	-	-	1.14	2.0
Cluster	1.27	2.0	1.14	2.0	1.14	2.0

### Phase Locked Loop (PLL)

Grid-feeding PV systems are synchronized with the rest of the microgrid using PLL [35,39]. The block diagram of the PLL comprising a PI controller and a controlled plant is illustrated in Figure 6. In the steady-state, the voltage signal  $v_q$  is equal to zero.

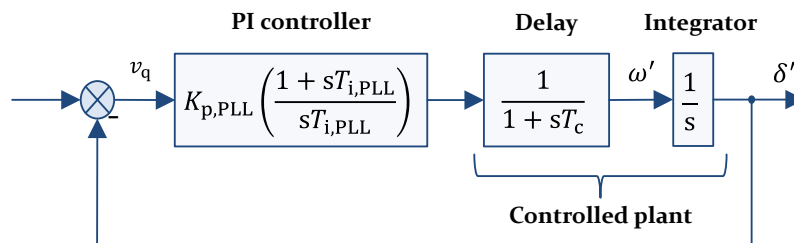


Figure 6. Block diagram of the phase locked loop in PV, according to [39].

As a result of the integrator block in the controlled plant, symmetrical optimum was employed for dimensioning the controller parameters:  $K_{p,PLL}$  and  $T_{i,PLL}$ . The corresponding formulae are shown in Equation (3). The variation factor is given by  $b = 1/\omega_{co}T_{pwm}$ , where  $\omega_{co}$  is the crossover frequency.  $V_n$  is the nominal grid voltage in pu, i.e., per unit. [39]

$$\begin{aligned} K_{p,PLL} &= \frac{1}{bV_nT_{pwm}} \\ T_{i,PLL} &= b^2T_{pwm} \end{aligned} \tag{3}$$

Table 6 lists the calculated controller parameters of the PLL in PV systems. The values are identical in each PV, since the parameters are independent of the grid connection point.

**Table 6.** Values of  $K_{p,PLL}$  and  $T_{i,PLL}$  in the phase locked loop of PV.

	$K_{p,PLL}$	$T_{i,PLL}$
<b>PV A.1</b>		
<b>PV B.1</b>	314	0.0101
<b>PV C.1</b>		

### 2.3.2. Battery Storage Systems

The block diagram of BSS with grid-forming inverter, which can be operated in parallel mode with other generators, is shown in Figure 7. Hence, the PLL is absent in the control loops. Neglecting the DC-side dynamics of BSS, the control structure comprises of three controllers: current, voltage (AC) and droop controller. The current and voltage controller represents the inner and outer control loop, respectively. [36,40,41] In the droop controller, there exists a correlation between active and reactive power with angle  $\delta'$  and the input signal  $v'_{ref}$  [42]. The details of the grid-forming inverters will not be dealt with in this paper.

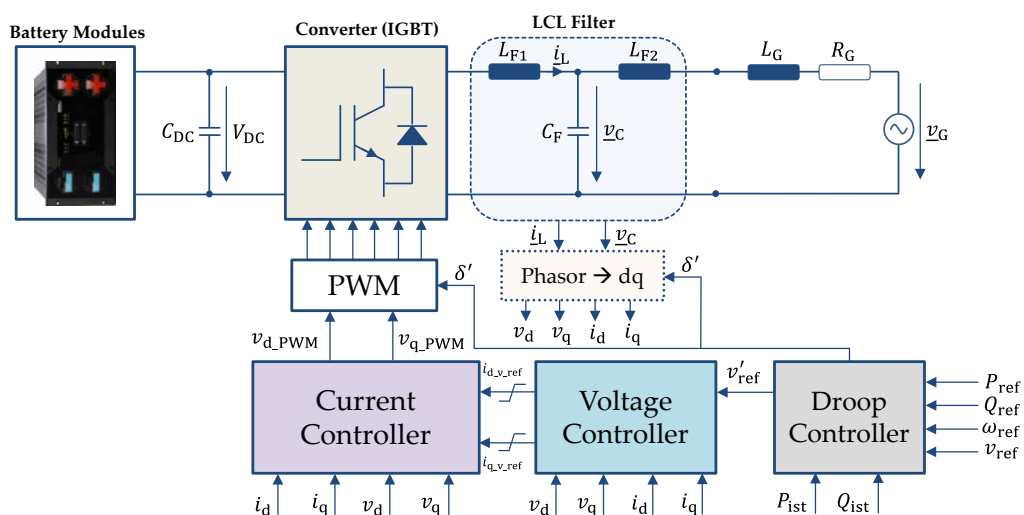


**Figure 7.** Block diagram of grid-forming BSS with corresponding controllers, according to [36,42].

In the steady-state operating conditions, the grid-forming inverters act as voltage sources. However, the inverters behave as controlled current sources in case of short-circuits. [41] This is due to the fact that, the input signals of the current controller are limited to a maximum value of 1 pu with the help of a current limitation block. Hence, the output current of BSS will be not greater than the nominal value. [41,43] It should be noted that, virtual impedance strategy, described in [36,41], leads to frequent spikes in the output current, which is unfavorable in microgrids in case of short-circuits.

### Current Controller

The block diagram of the inner control loop is identical to that of PV (see Figure 4). The Bode plots and the step response of the transfer functions were acceptable. The parameters in the current controller of BSS were calculated using Equation (1). The corresponding values are listed in Table 7.

**Table 7.** Values of  $K_{pc}$  and  $T_{ic}$  in the current controller of BSS of scenario “storage” with respect to the operating modes.

	BSS A.1		BSS B.1		BSS C.1	
	$K_{pc}$	$T_{ic}$	$K_{pc}$	$T_{ic}$	$K_{pc}$	$T_{ic}$
<b>Island</b>	-	-	-	-	0.60	0.0012
<b>Interconnection</b>	0.76	0.0012	-	-	0.55	0.0012
<b>Cluster</b>	0.68	0.0012	0.50	0.0012	0.50	0.0012

### AC Voltage Controller

Figure 8 shows the block diagram of the voltage controller in grid-forming BSS. The controlled plant comprises, among others, the integrator block due to the filter capacitance. Hence, symmetrical optimum was applied to determine the control parameters:  $K_{pv}$  and  $T_{iv}$ . [37,41,44] The Bode plots and the step response of the transfer functions for  $a$  equal to 4 were acceptable and the control system was accessed to be stable.

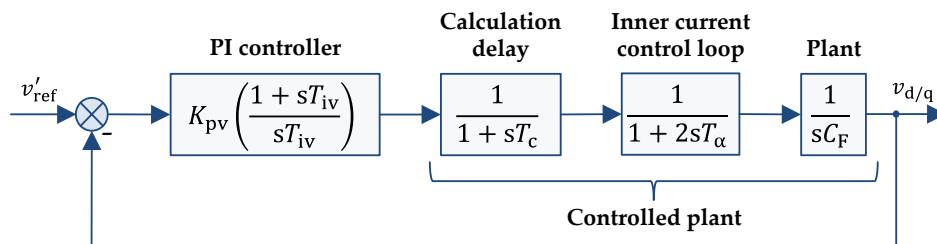


**Figure 8.** Block diagram of the outer control loop in BSS, according to [44].

The calculation of the control parameters was performed with the help of Equation (4), where  $C_F$  and  $T_\gamma$  represents the filter capacitance and the summation of time delays, respectively. [41,44]

$$\begin{aligned}
 K_{pv} &= \frac{C_F}{aT_\gamma} \\
 T_{iv} &= a^2T_\gamma
 \end{aligned}
 \tag{4}$$

Long-lasting oscillations were observed in grid simulations for the calculated values of  $K_{pv}$  and  $T_{iv}$ —like in PV systems. Hence,  $K_{pv}$  and  $T_{iv}$  were exemplarily multiplied by a factor of 1.5 and 3000, respectively. Consequently, no oscillations were noticed. Table 8 lists the values of the parameters in the voltage controller of BSS in scenario “storage” regarding the three different operating modes.

**Table 8.** Values of  $K_{pv}$  and  $T_{iv}$  in the voltage controller of BSS of scenario “storage” with respect to the operating modes.

	BSS A.1		BSS B.1		BSS C.1	
	$K_{pv}$	$T_{iv}$	$K_{pv}$	$T_{iv}$	$K_{pv}$	$T_{iv}$
<b>Island</b>	-	-	-	-	0.63	8.4
<b>Interconnection</b>	0.91	8.4	-	-	0.63	8.4
<b>Cluster</b>	0.91	8.4	0.63	8.4	0.63	8.4

#### 2.4. Fault Behaviour of Microgrids in the Island Mode

Before performing dynamic short-circuit analysis, microgrid C, along with the other two microgrids, in the islanded mode was verified according to the ISO norm 8528-5 [32,33] with respect to the five scenarios—both in the steady-state and with sudden step-load change. The latter is performed by increasing as well as decreasing the actual power consumption of the static loads—at the studied operating point—up to 40% and 90%, respectively. According to [17], a significant reduction in the solar irradiance of ca. 55% within 2.5 s does not have negative consequences in the analyzed clustered microgrid model comprising DG and PV, which is similar to the microgrid model in scenario “sun”.

The three-phase fault location in microgrid C in scenario “storage” (representing all the installed grid equipment) is shown in Figure 9. Since the short-circuit location is very close to a DG and a grid-forming BSS, the fault is assumed to be critical. The fault clearance is achieved by tripping the affected line only, i.e., L C.5, with the help of differential protection. The clearing time is identical in each scenario and corresponds to the minimum value of the CCT among the scenarios. It should be noted that, in this research work the resistance of the fault was assumed to be 0.02  $\Omega$ .

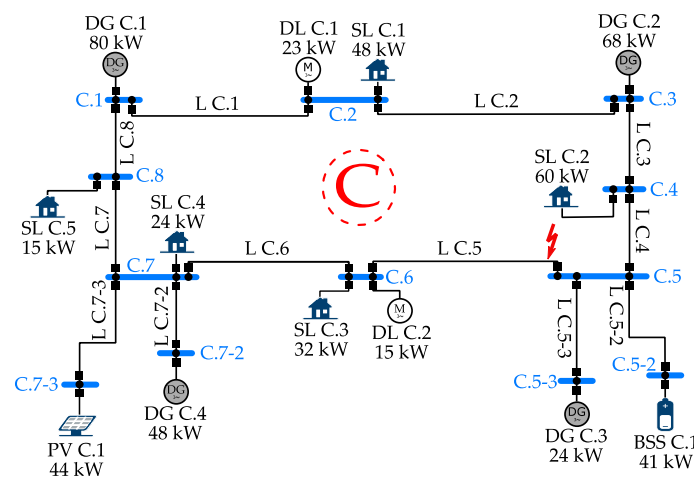


**Figure 9.** Microgrid C in the islanded mode (scenario “storage”) with the investigated fault location.

If the bus voltage drops below 0.15 pu, inverter-based systems can be disconnected from the system according to [45]. Further, DGs can be tripped in case of a voltage drop of 0.3 pu or less [45]. However, DGs, PV, and BSS were purposely not disconnected in this research work—irrespective of the bus voltage. On the other hand, induction motors, i.e., dynamic loads, were tripped 40 ms after the fault occurrence using undervoltage protection [46]. Soon after the fault incident, induction motors will provide subtransient short-circuit currents (similar to DGs), which are beneficial also in microgrids. However, the reactive power demand of induction motors during the fault-on and the post-fault time period can be very critical in microgrids and also can lead to voltage or system collapse.

The short-circuit behavior of the classical and the hybrid microgrids in the islanded mode was studied—before performing qualitative and quantitative TSA—not only at the system level, but also at the equipment level. First and foremost, the measured voltage and frequency on the buses were compared regarding the scenarios. The considered variables of DGs are relative rotor angle (i.e., rotor angle in the center of inertia frame, COI), actual rotor angular frequency, and relative rotor angular frequency deviation. Furthermore, electrical and mechanical torque of DGs were also analyzed taking “storage” and “sun & storage” (comprising DGs, PV, and BSS) into account.

The active and reactive power as well as the output current of DGs, PV, and BSS were also investigated. The profiles of the static and dynamic loads will not be shown in this paper. By analyzing the system and the equipment behavior under short-circuit conditions, the modelling of the classical and hybrid microgrids were verified and also compared with each other.

### 2.5. Effect of Pooling Microgrids on the System Stability

The influence of coupling microgrids on the system stability should be analyzed not only qualitatively, but also quantitatively. It has been already mentioned that only microgrid C was studied in the islanded mode. The interconnected mode corresponds to microgrid A and C, whereas the ring topology of microgrid A, B, and C was considered in the clustered mode. It should be noted that the power exchange between the microgrids in the coupled operating modes was negligible. These three operating modes along with five scenarios lead to 15 different grid models, in other words 15 different cases. Henceforth, other combinations of the microgrids were not considered in this research work.

Firstly, the *CCT* of microgrids with respect to the 15 cases were calculated by performing RMS-simulations (fault on lines) with a fault resistance of  $0.02 \Omega$ . This allows to compare the *CCT* values with respect to the scenarios and operating modes, so that the sensitivity of the microgrids can be assessed in terms of transient stability. The methodology of the calculation of the *CCT* has been given in [20]. The *CCT* values were categorized according to Table 9. The minimum feasible clearing time (differential protection) in the studied microgrids is approximately 60 ms [47–50].

**Table 9.** Classification of the *CCT* in the studied microgrids.

<i>CCT</i> Range	Risk Level
less than 60 ms	extreme
60–100 ms	very high
101–150 ms	high
151–200 ms	medium
201–300 ms	low
greater than 300 ms	very low

Secondly, the behavior of microgrids in the case of the three-phase fault in microgrid C (illustrated in Figure 9) was investigated in detail. In contrast to the analysis in the islanded mode, the individual variables and parameters of the grid equipment will not be shown. In this research, work voltage and frequency stability will be analyzed along with rotor angle stability.

### 2.6. Quantitative Transient Stability Assessment

In the 1990s, five hybrid methods were proposed for quantitative TSA in transmission systems combining the advantages of TDS and TEF [51–55]. These techniques have been discussed in [19], which cannot be employed in microgrids comprising engine-driven synchronous generators with relatively fast reacting speed governor. Hence, a new hybrid method has been proposed in [19], which has been improved in [20]. This hybrid technique valid for microgrids is called “the micro-hybrid method”. Figure 10 lists the hybrid methods to quantitatively assess the transient stability of electrical energy systems.

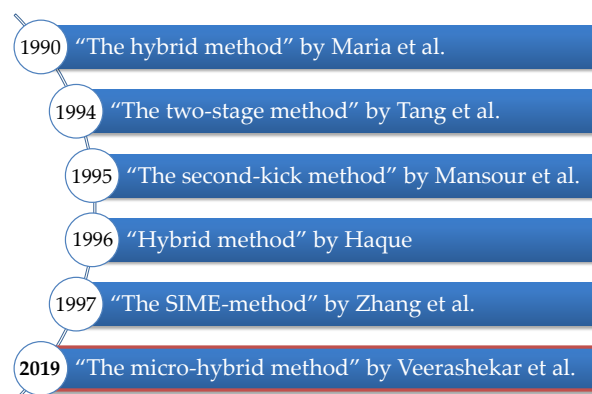


**Figure 10.** Overview of the hybrid methods for quantitative TSA.

Using the micro-hybrid method, three stability related terms can be determined, namely system stability degree (SSD) as well as stability reserve degree (SRD) and participation factor (PF) of individual synchronous generators. The corresponding results of the TDS can be analyzed further with the help of the TEF given in Equation (5).  $E$ ,  $E_{kin}$ , and  $E_{pot}$  represents the total energy, kinetic energy (KE), and potential energy (PE), respectively. The detailed derivation, based on [22,56], can be found in [19,20].

$$E = \sum_{i=1}^n H_i \omega_n \Delta \omega_{iCOI,pu}^2 - \sum_{i=1}^n \int_{\delta_{iCOI_0}}^{\delta_{iCOI_1}} \tau_{iCOI\Sigma,pu} d\delta_{iCOI} \quad (5)$$

$$E_{kin} = \sum_{i=1}^n H_i \omega_n \Delta \omega_{iCOI,pu}^2 \quad \text{and} \quad E_{pot} = \sum_{i=1}^n \int_{\delta_{iCOI_0}}^{\delta_{iCOI_1}} \tau_{iCOI\Sigma,pu} d\delta_{iCOI}$$

$H_i$ ,  $\omega_n$ , and  $\Delta \omega_{iCOI,pu}$  are the inertia constant of the  $i$ -th synchronous generator, nominal rotor angular velocity, and change in the rotor angular velocity in the COI frame, respectively. On the other hand,  $\delta_{iCOI_0}$  and  $\delta_{iCOI_1}$  represents the pre-fault and post-fault rotor angle of the  $i$ -th synchronous generator, respectively. Further, the rotor angle of each generator in the COI frame is given by  $\delta_{iCOI}$ .  $\tau_{iCOI\Sigma,pu}$  describes the equivalent torque of the individual generators in the COI frame (see Equation (6)).

$$2H_i \frac{d\Delta \omega_{iCOI,pu}}{dt} = \tau_{mi,pu} - \tau_{ei,pu} - \frac{H_i}{H_\Sigma} \tau_{COI,pu} = \tau_{iCOI\Sigma,pu} \quad (6)$$

$\tau_{mi,pu}$  and  $\tau_{ei,pu}$  represent the mechanical and electrical torque of the  $i$ -th synchronous generator, respectively. The summation of the inertia constant of each generator is given by  $H_\Sigma$ . Equation (7) describes the equivalent torque of the COI reference machine  $\tau_{COI,pu}$ , where  $\Delta \omega_{COI,pu}$  is the change in the rotor angular velocity of the COI reference machine.

$$\tau_{COI,pu} = 2H_\Sigma \frac{d\Delta \omega_{COI,pu}}{dt} = \sum_i \tau_{mi,pu} - \tau_{ei,pu} \quad (7)$$

The methodology of the calculation of the KE and PE has been explained in detail in [19,20]. Based on the energy values of all the generators until the point of time corresponding to the end of the forward swing of the critical generator, the critical energy  $E_{cr}$  and clearing energy  $E_{cl}$  can be calculated [19,20].  $E_{cr}$  and  $E_{cl}$  correspond to the CCT and (stable) fault clearing time, respectively. Due to a large number of investigated cases (15 in total) regarding operating modes and scenarios, only the SSD has been taken into account in this research work, which is given by Equation (8). SSD defines the percentage margin of a microgrid towards instability boundary for a (stable) fault clearing time, e.g., SSD of 75% indicates that the microgrid has a reserve of 75% with respect to the rotor angle stability. In other words, the microgrid has lost 25% of its stability reserve.

$$SSD = \frac{E_{cr} - E_{cl}}{E_{cr}} \cdot 100 \% \quad (8)$$

In [20], the threshold value of the SSD to determine the corrected critical clearing time (CCCT) was discussed. Since a microgrid cannot be modelled without any inaccuracies and assumptions, a SSD-threshold of 10% can be assumed. As a result, the new CCT, i.e., CCCT, can be considered as the maximum allowable time to clear the fault.

Furthermore, the critical energy of the system  $E_{cr}$  and the critical machine  $E_{cr,cm}$  were analyzed taking the CCT into consideration. In a one-machine infinite bus system, the CCT is inversely proportional to the critical energy. The correlation between these critical energies and the CCT was studied regarding the operating modes and scenarios. Similarly, the effect of the fault location on the critical energy was analyzed in the clustered mode with respect to the three-phase fault on both ends of L C.5, i.e., very close to busbar (BB) C.5 and C.6.

### 3. Results and Discussion

The results of the performed simulations will be presented and discussed in this section. Firstly, the CCT profile of the different operating modes and scenarios will be described in Section 3.1. The next section (Section 3.2) deals with the system behavior under fault conditions in island mode. Consequently, the influence of coupling microgrids on the voltage, the frequency, and the rotor angle stability will be qualitatively analyzed in Section 3.3. Furthermore, the profiles of the SSD versus clearing times—based on the quantitative TSA using the micro-hybrid method—will be discussed in Section 3.4 with respect to the operating modes and scenarios. The last two sections (Sections 3.5 and 3.6) deal with the critical energy of the system and critical machine.

#### 3.1. Critical Clearing Times

##### 3.1.1. Comparison of Scenarios

In this section, the percentage distribution of CCT values of the various scenarios with respect to the islanded mode (microgrid C), interconnected mode (microgrid A and C), and clustered mode (microgrid A, B, and C) will be discussed—see Figure 11. It has been mentioned in Section 2.3 that faults were simulated on lines within each microgrid except tie-lines. The categorization and comparison of the CCT values is based on Table 9.

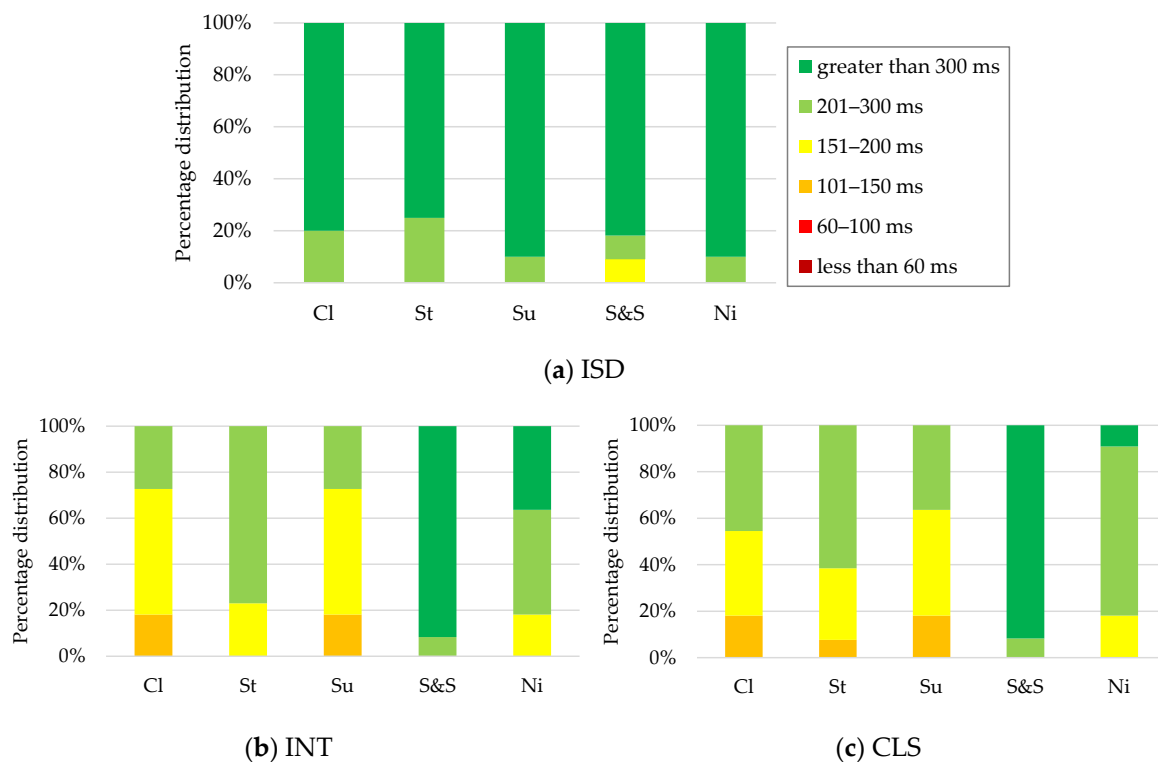


**Figure 11.** Percentage distribution of CCT with respect to different scenarios in: island (a), interconnection (b), and cluster (c) mode.

#### Island

Figure 11a corresponds to the islanded mode (i.e., microgrid C). The risk level of the majority—approximately 80%—of the CCT values in each scenario is very low ( $CCT > 300$  ms). In scenario “sun & storage” with DGs, PV, and BSS (acting as generating units), several CCT values correspond to the risk level belonging to medium, which is considered to not be critical. In the following subsections, the CCT profile of the interconnected and clustered mode will be discussed.

### Interconnection

According to Figure 11b, the risk level corresponding to extreme ( $CCT < 60$  ms) and very high ( $CCT$  between 60–100 ms) has not been observed in any of the scenarios in the interconnected mode. However, expect in scenario “sun & storage” the risk level varies between high and very low. The risk of one of the DGs losing synchronism with the system is higher in the interconnected mode.

### Cluster

Figure 11c shows that the  $CCT$  profile of each scenario is almost identical to that of the interconnected mode—cf. Figure 11b. Scenario “sun & storage” can be highly recommended in the interconnected and clustered mode, whereas any scenario can be preferred in the islanded mode.

Considering a three-phase fault on line L C.5 (see Figure 9), an in-depth analysis of the effect of coupling off-grid microgrids on the system stability will be performed in Section 3.3. In the next section, a quantitative comparison of the  $CCT$  profiles will be performed taking only microgrid C into account.

### 3.1.2. Comparison of Scenarios with Respect to Operating Modes

#### Interconnection vs. Island

With the help of Equation (9), the  $CCT$  of 11 overhead lines in microgrid C has been quantitatively compared regarding the interconnected and islanded mode.  $\Delta CCT$ ,  $CCT_{INT}$ , and  $CCT_{ISD}$  correspond to the relative  $CCT$  difference in percentage, absolute  $CCT$  value (ms) in the interconnected mode and islanded mode, respectively.

$$\Delta CCT = \frac{CCT_{INT} - CCT_{ISD}}{CCT_{ISD}} \cdot 100 \% \tag{9}$$

It can be observed in Figure 12 that except scenario “sun & storage” a negative difference is characterized in each scenario. The maximum positive and negative difference lies around +40% and −80%, respectively. The fault on line L C.5—close to a DG and BSS, and with a  $CCT$  change of roughly +10% and −70%—will be investigated in the further sections.

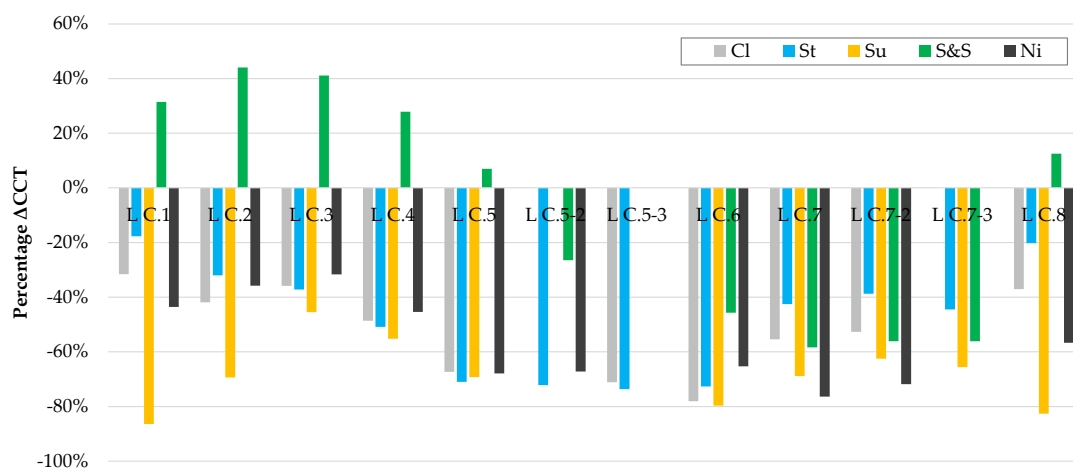
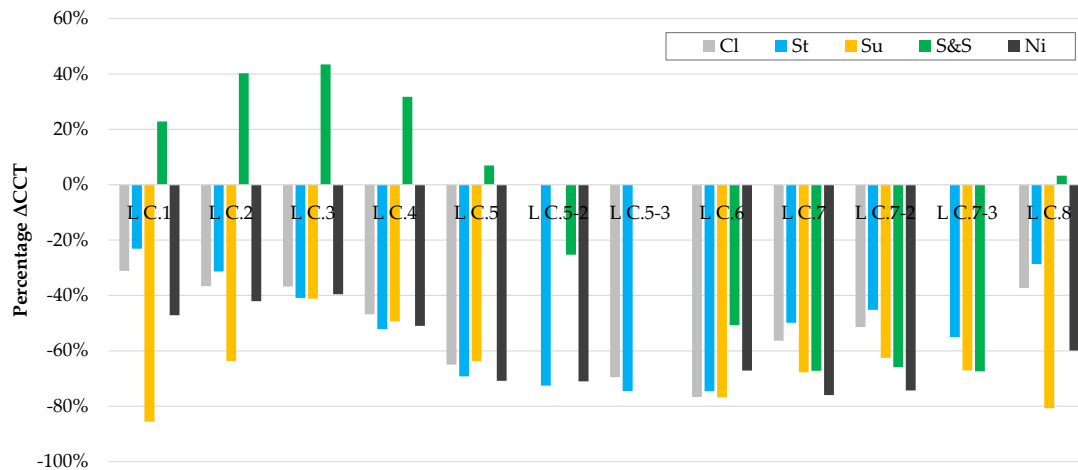


Figure 12. Relative percentage difference of  $CCT$  of microgrid C in interconnection and island mode.

### Cluster vs. Island

Since the  $CCT$  profiles are nearly similar in the coupled microgrids, the comparison has been performed—between the clustered and islanded mode—using Equation (10). According to Figure 13, the  $\Delta CCT$  values of microgrid C remain almost identical to the values illustrated in Figure 12.

$$\Delta CCT = \frac{CCT_{CLS} - CCT_{ISD}}{CCT_{ISD}} \cdot 100 \% \quad (10)$$



**Figure 13.** Relative percentage difference of CCT of microgrid C in cluster and island mode.

### 3.1.3. Comparison of Operating Modes

For the TSA in the grid planning phase and/or grid operation, not only different points of time (i.e., scenarios) are essential, but also different operating modes. Hence, the  $CCT$  profiles will be presented according to the scenarios—taking solely microgrid C into consideration—so that different operating modes can be compared directly.

#### Classical

Figure 14a represents the percentage distribution of  $CCT$  in the classical scenario of microgrid C regarding the islanded, interconnected, and clustered mode. The other profiles in Figure 14 correspond to the hybrid scenarios.

In case of microgrids comprising DGs only, the choice of the optimal operating mode can be easily made based on Figure 14a: island over pooling. However, coupling the microgrid with neighboring microgrids is not characterized by unacceptable  $CCT$  values.

#### Hybrid

In scenarios “storage” and “sun”, i.e., Figure 14b,c, island operation can be preferred to coupling modes for microgrid C. However, cluster mode can be favored in scenario “sun & storage” (cf. Figure 14d). The choice can be made between the islanded and interconnected mode in scenario “night” (cf. Figure 14e) from the microgrid C’s point of view.

In general, scenario “sun & storage” can be preferred to other scenarios in the interconnected and clustered mode. On the other hand, the selection of scenarios is not critical in the islanded mode. Furthermore, coupling classical or hybrid microgrids does not pose serious problems regarding transient stability, whereas the stability risk in the pooled modes is higher as against the islanded mode. However, the effect of extended coupling of microgrids (with different topologies) on the  $CCT$  values needs further investigations.

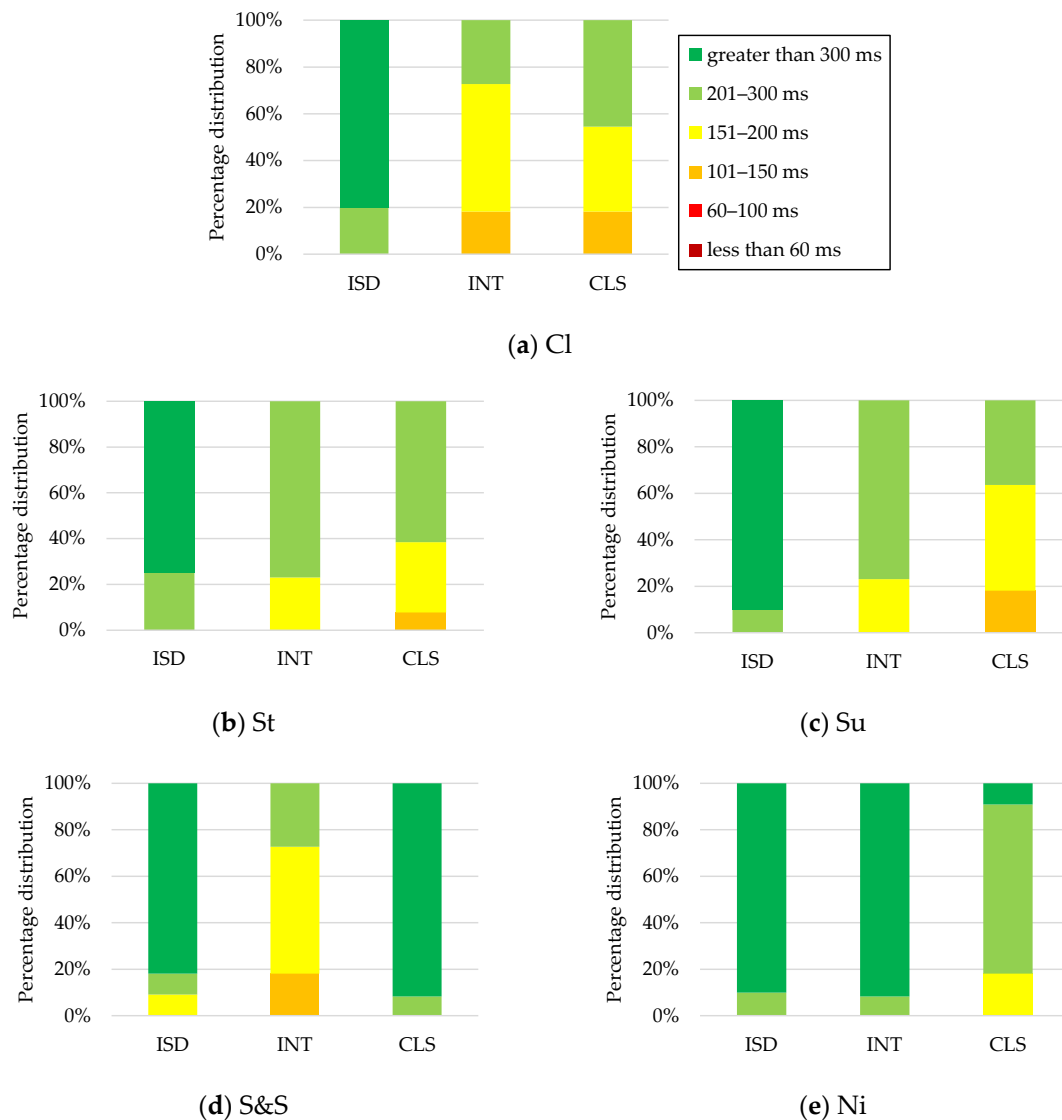


**Figure 14.** Percentage distribution of CCT in microgrid C with respect to different operating modes in: classical (a), storage (b), sun (c), sun and storage (d), and night (e) scenario.

### 3.2. Fault Behaviour of Microgrid C in Island Mode

Before investigating the fault behavior of the coupled classical and hybrid microgrids, the response of microgrid C at both system and equipment level, will be studied. Further, the microgrid modelling can be verified by analyzing the system and equipment profiles in the pre-fault, fault-on, and post-fault period.

The fault clearing time was chosen such that it corresponds to the minimum CCT of the scenarios. The CCTs of the scenarios in the ascending order is as follows: sun and storage (531 ms), classical (588 ms), sun (667 ms), storage (793 ms), and night (1058 ms). Hence, the fault on line L C.5 (see Figure 9) is cleared after 531 ms.

#### 3.2.1. Bus Voltage and Frequency

Figure 15 shows the voltage profiles of the busbars (BB) in microgrid C for different scenarios. Due to the relatively smaller dimension of microgrid C, voltage at all the busbars drops significantly soon after the fault incident. It should be noted that induction motors were disconnected 40 ms after the fault occurrence. The resulting voltage fluctuation (marginal increase) is negligibly small. During

the fault-on period, i.e., until the fault clearance, the corresponding bus voltages are almost similar in each scenario. Further, the post-fault voltage recovery is relatively quick—within about 1 s—in both the classical and hybrid scenarios. The influence of the employment of PV and BSS (hybrid scenarios) is not significant in the islanded mode of the studied microgrid C.

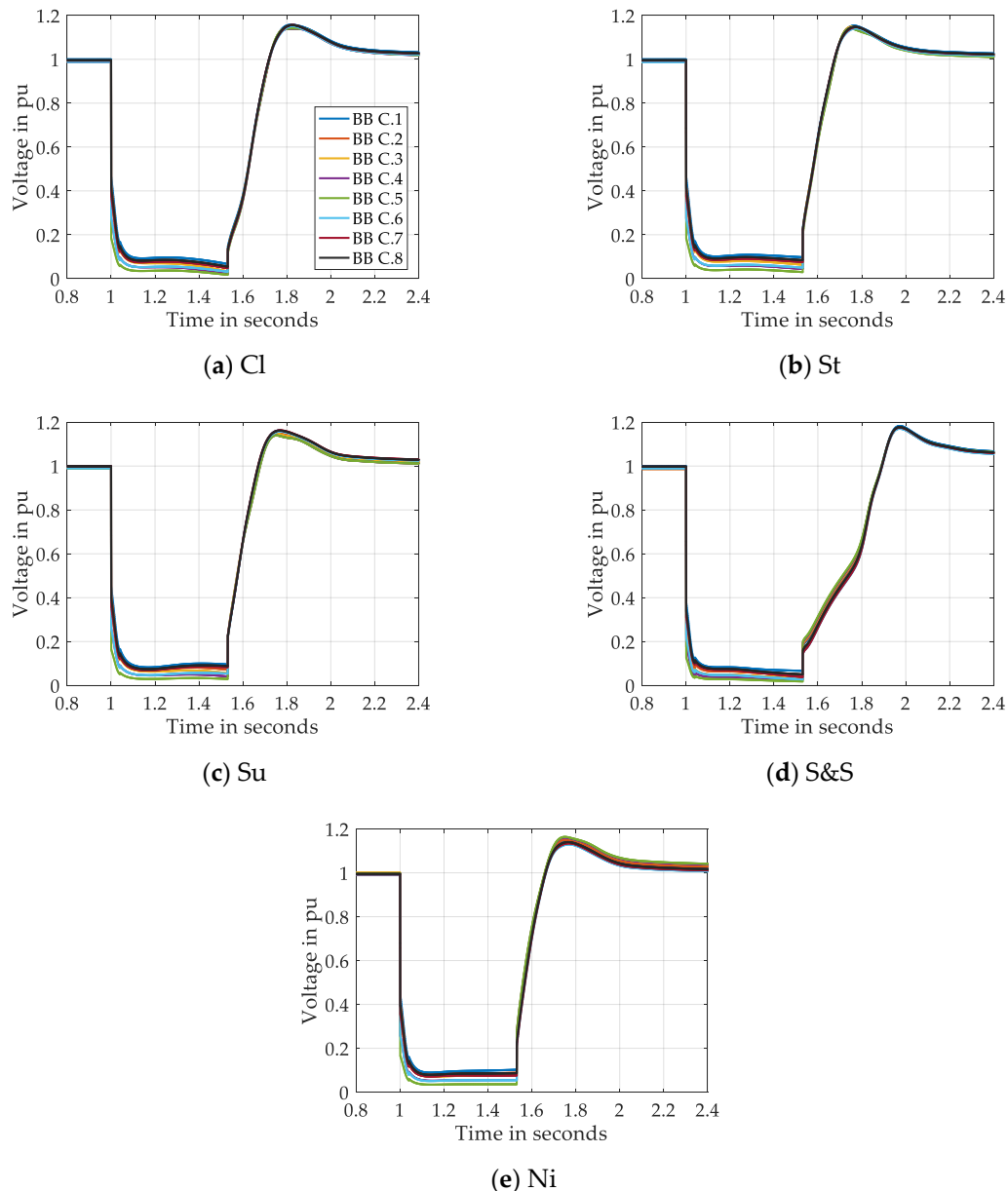


**Figure 15.** Voltage of busbars of microgrid C (island mode) in: classical (a), storage (b), sun (c), sun and storage (d), and night (e) scenario.

The observed frequency at the busbars of microgrid C of each scenario is illustrated in Figure 16. The minimum and maximum frequency in every scenario, except “sun & storage” is 45 Hz and 55 Hz, respectively—i.e.,  $\pm 10\%$  of the nominal value. The frequency range in “sun & storage” with 2 DGs is between 43 Hz and 57 Hz ( $\pm 14\%$ ). The frequency drops significantly in the subtransient phase due to the provision of very high short-circuit current/power by the DGs. The frequency fluctuation due to the disconnection of induction motors 40 ms after the fault incident is noticeable, however not critical. During fault-on period, the frequency values lie in the overfrequency range (greater than 50 Hz) as a

result of the very fast reaction of the speed governor of the DGs. This will be discussed more in the following subsections.

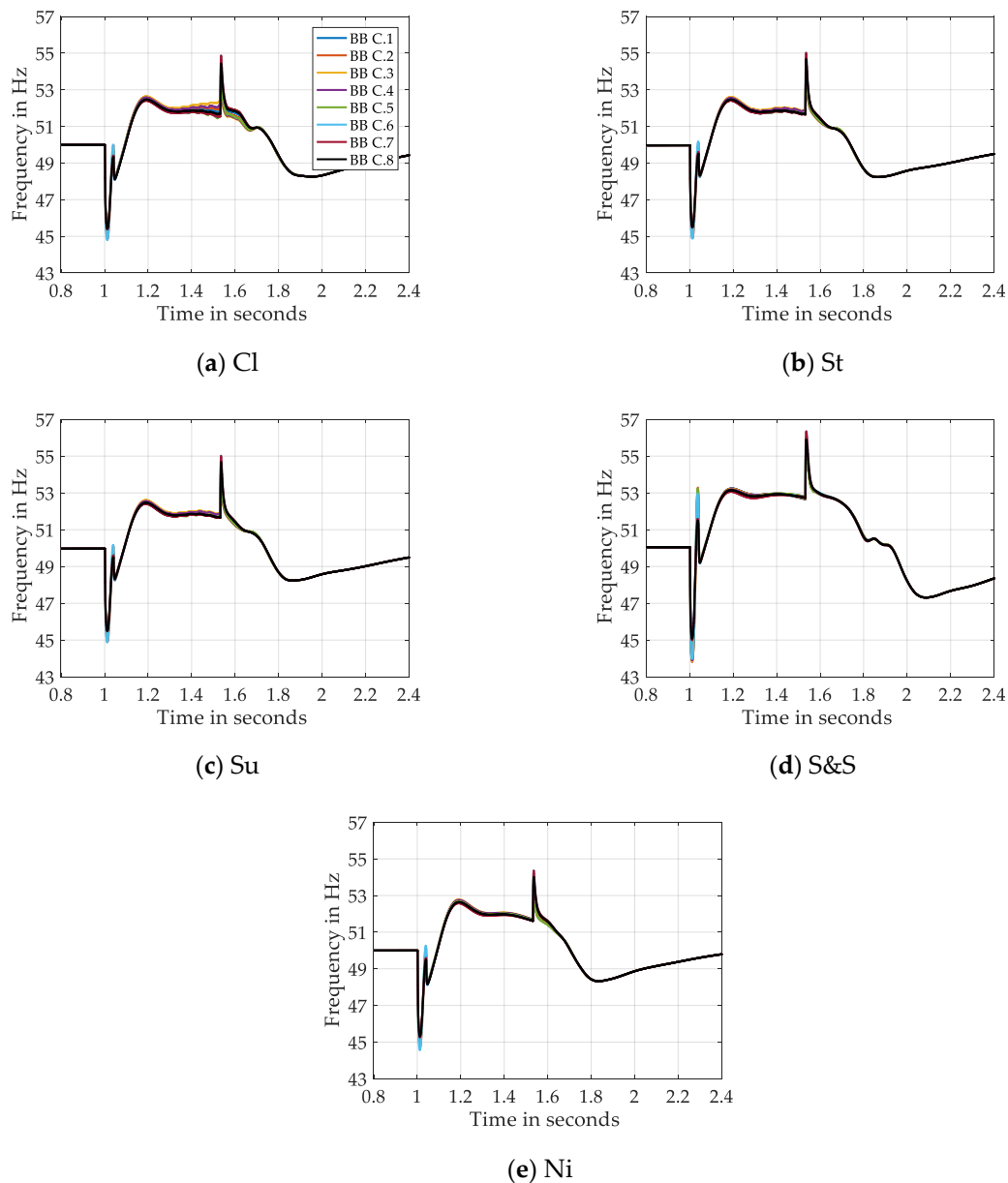


**Figure 16.** Frequency of busbars of microgrid C (island mode) in: classical (a), storage (b), sun (c), sun and storage (d) and night (e) scenario.

A sharp frequency increase is noticed in each scenario soon after the fault clearance, which is as a result of the positive difference between the total generation and load in the microgrid. The frequency recovery in the post-fault period lasts only about 1 s. Due to the disconnection of the induction motors and absence of secondary frequency control (in principle not necessary for stability analyses) in the studied microgrids, the steady-state frequency in the post-fault period is approximately equal to 50 Hz and not exactly 50 Hz.

### 3.2.2. Relative Rotor Angle, Actual Rotor Angular Frequency and Relative Rotor Angular Frequency Deviation of DGs

#### Relative Rotor Angle

The rotor angle of the DGs in microgrid C of each scenario in the COI reference frame is depicted in Figure 17. The list of the active DGs in every scenario is shown in Table 3. The critical machine is DG C.2 in all the scenarios except in scenario “sun & storage”, where DG C.1 loses synchronism. Even though scenario “sun & storage” has the minimum CCT (corresponding to the clearing time), the observed value of the rotor angle of the critical machine is slightly higher than  $80^\circ$ . In general, the end of the forward and backswing of the DGs in each scenario occurs almost at the same point of time.

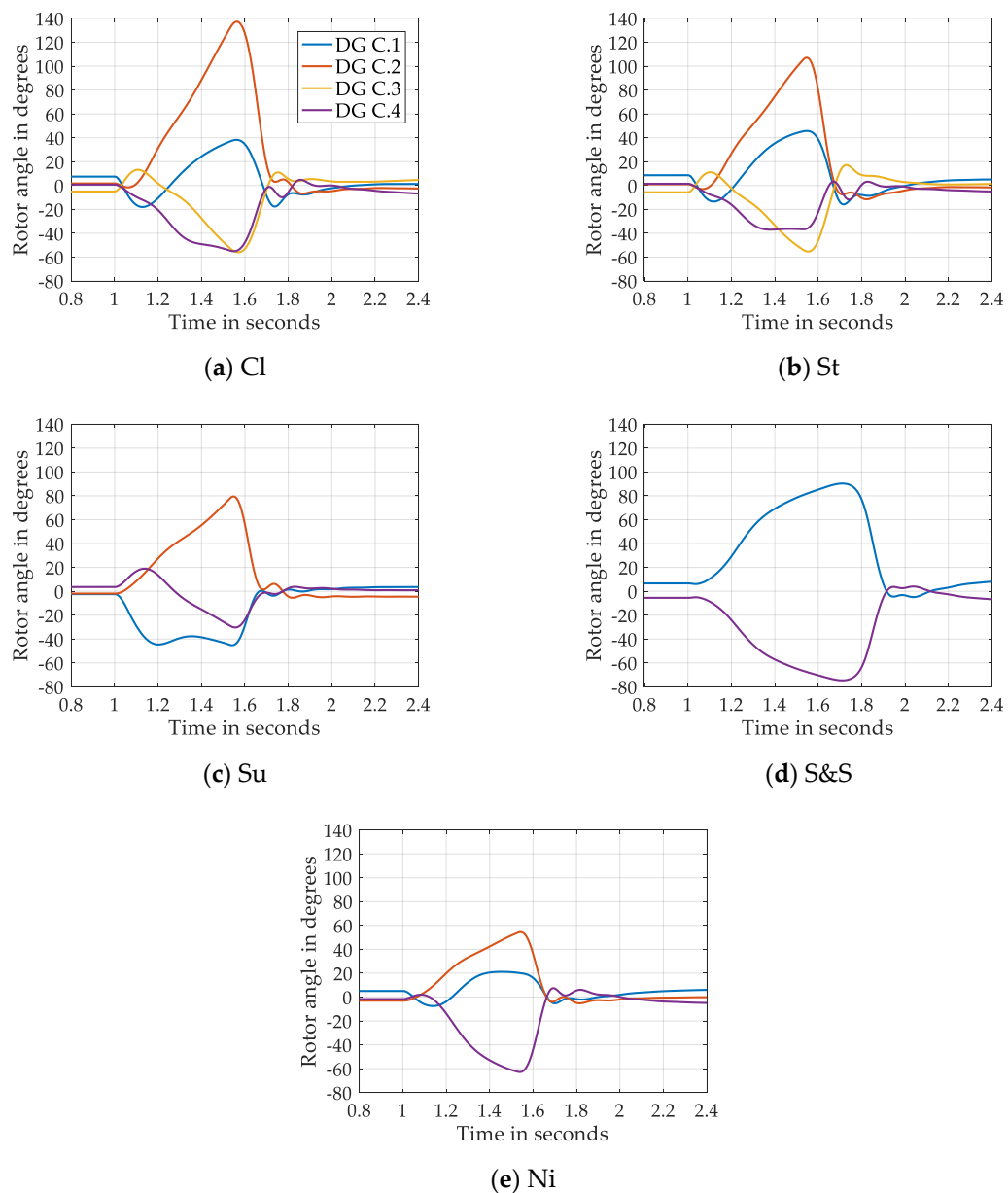


**Figure 17.** Relative rotor angle of DGs of microgrid C (island mode) in: classical (a), storage (b), sun (c), sun and storage (d) and night (e) scenario.

### Actual Rotor Angular Frequency

Figure 18 illustrates the actual rotor angular frequency of the DGs in microgrid C of each scenario. Soon after the fault incident, the speed of the rotors drops due to the provision of (subtransient) short-circuit currents by DGs. As a result of the decrease in the magnitude of the short-circuit currents and increase in the mechanical moment of the speed governor during the fault-on period, the rotor angular frequency of the DGs increases. The DGs regain synchronism within roughly 500 ms after the fault clearance. In scenarios with the maximum number of DGs, i.e., classical and storage, relatively larger oscillations can be noticed.

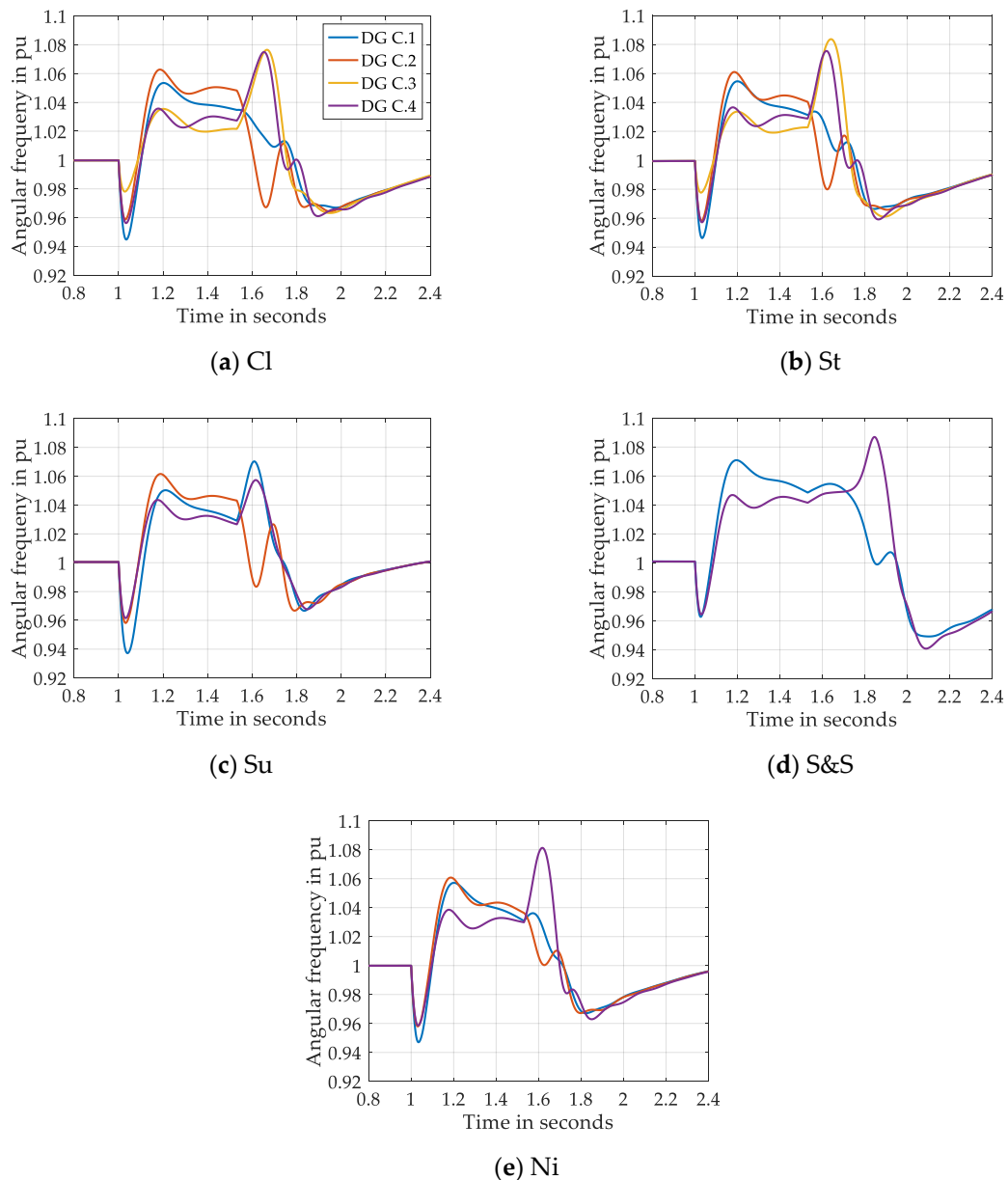


**Figure 18.** Actual rotor angular frequency of DGs of microgrid C (island mode) in: classical (a), storage (b), sun (c), sun and storage (d), and night (e) scenario.

### Relative Rotor Angular Frequency Deviation

The relative rotor angle of the DGs is directly related to their relative rotor angular frequency deviation (see Figure 19), which is also represented in the COI reference frame. It can be observed

that the DGs with the rotor acceleration during the fault-on period exhibit deceleration soon after the fault clearance, and vice-versa. The maximum relative rotor angle (see Figure 17) is noticed just after clearing the fault, where the rotor angle deviation is predominantly due to the rotor acceleration. The rotor angle increases further—only slightly—after tripping the faulty line as a result of the rotor deceleration. The negative relative angular frequency of the critical machine corresponds to the sharp decrease in the rotor angle.

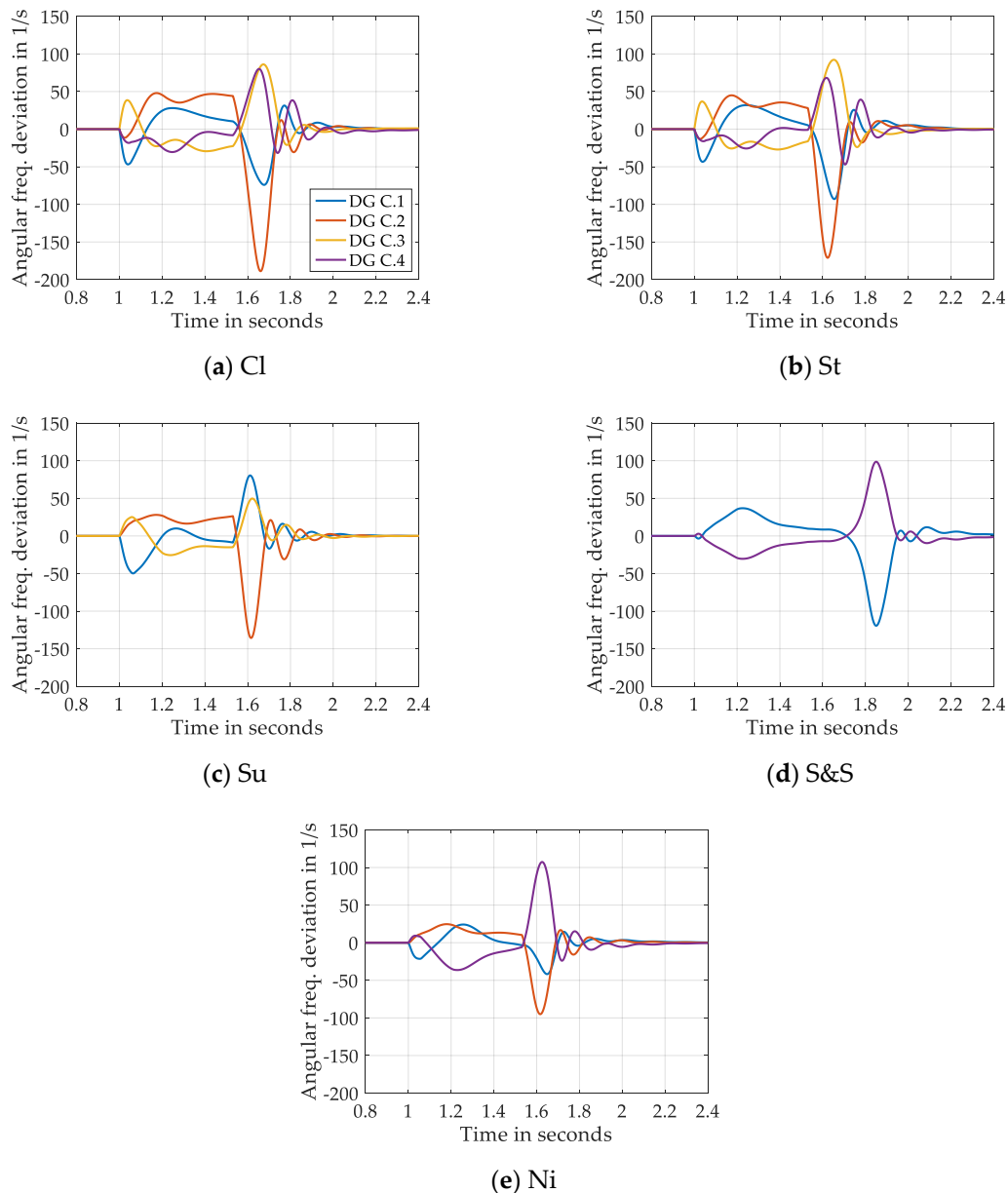


**Figure 19.** Relative rotor angular frequency deviation of DGs of microgrid C (island mode) in: classical (a), storage (b), sun (c), sun and storage (d), and night (e) scenario.

- Electrical and Mechanical Torque of DGs

In the following subsections, the scenarios “storage” and “sun & storage” will be considered, where the BSS acts as a load and a generation unit, respectively. Further, these two scenarios—representing DGs, PV, and BSS being active—correspond to the maximum and minimum number of the DGs. Figure 20 illustrates the electrical (in principle, electromagnetic) torque of the DGs in microgrid C. The sharp increase of the torque—soon after the fault incident—corresponds to the subtransient

short-circuit current, which will be shown at the end of this section. Since the voltage drop in scenario “sun & storage” is slightly higher than in storage, the corresponding maximum torque of DG C.1 in scenario “sun & storage” is 3.5 pu, whereas the value is 2.6 pu in scenario “storage”. As a result of the (sustained) fault until the line tripping, a relatively smaller short-circuit current leads to an electrical torque of less magnitude.

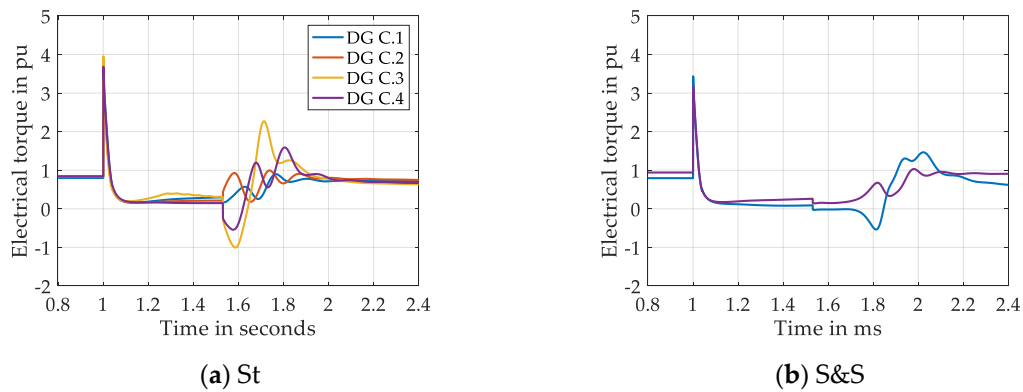


**Figure 20.** Electrical torque of DGs of microgrid C (island mode) in: storage (a) and sun and storage (b) scenario.

Several tens of milliseconds after the fault occurrence, the mechanical torque of the DGs will be increased by the speed governor DEGOV1 of the DGs due to the drop in the frequency (cf. Figure 21). In case of transmission systems, the speed governor in synchronous generators during fault-on period does not change the mechanical torque due to relatively large time constants (few seconds) [22]. However, the set point of torque/power can be changed very quickly in engine-driven generators. The maximum and the minimum limit of torque in DEGOV1 corresponding to 1 pu and 0 pu, respectively, can be observed in the profiles. Once the short-circuit current (electrical torque) of the DGs decreases, the difference between the mechanical and electromagnetic torque becomes positive, which causes an increase in the rotor speed. Consequently, the mechanical torque is reduced by DEGOV1 from 1 pu to almost 0 pu. After the fault clearance, the torque will be increased such that the speed deviation becomes zero.

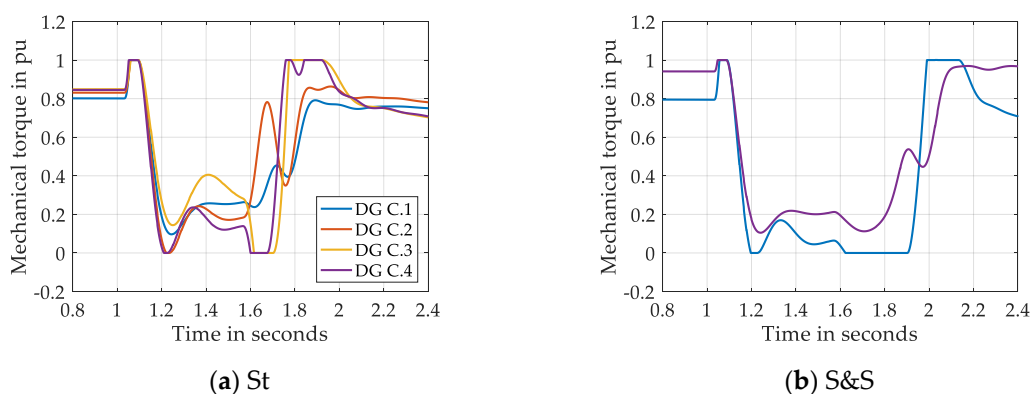


**Figure 21.** Mechanical torque of DGs of microgrid C (island mode) in: storage (a) and sun and storage (b) scenario.

- Active and Reactive Power as well as Output Current of DGs, PV, and BSS
  - Active Power

Since the voltage is nearly 0.1 pu during fault-on period, the electrical power is close to 0 pu. However, due to the residual voltage and very high short-circuit current in the subtransient phase the active power is significantly high—cf. Figure 22.

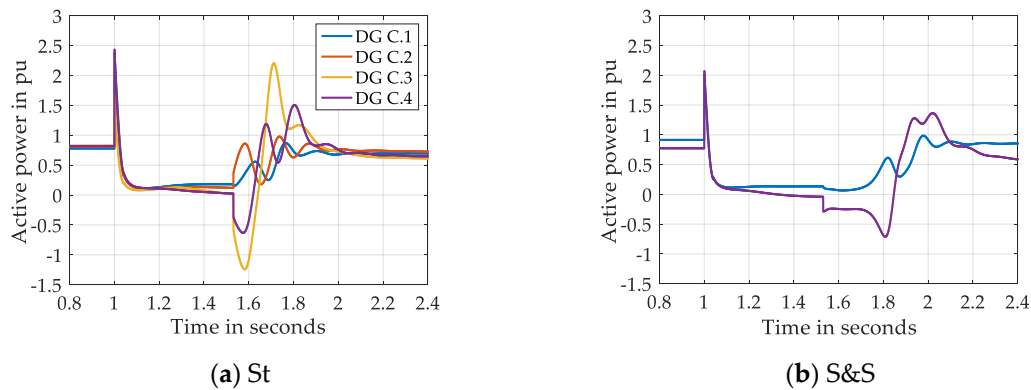


**Figure 22.** Real power of DGs of microgrid C (island mode) in: storage (a) and sun and storage (b) scenario.

The active power of the grid-feeding PV in scenario “storage” and “sun & storage” is shown in Figure 23. Unlike DGs the provision of the short-circuit current in PV is limited. Hence, the profile of the active power is significantly dependent on the terminal voltage. Due to the relatively slower (post-fault) voltage recovery in sun and storage, it takes slightly longer to reach the pre-fault value of the active power.

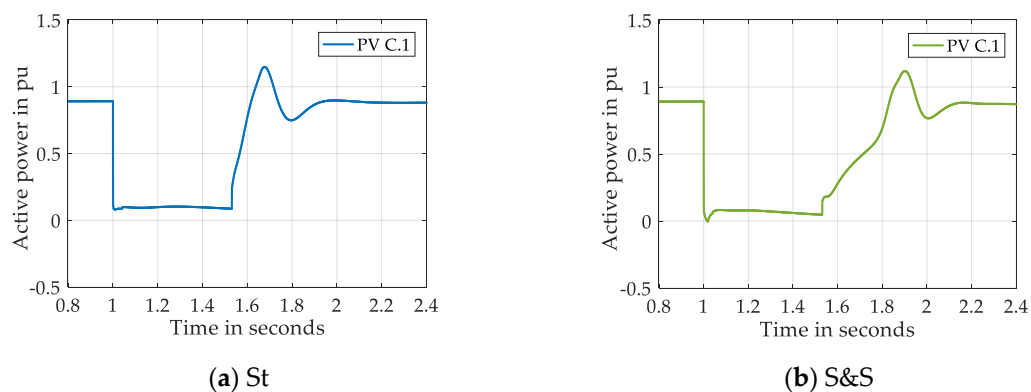


**Figure 23.** Real power of PV of microgrid C (island mode) in: storage (a) and sun and storage (b) scenario.

Figure 24 illustrates the active power of the grid-forming BSS, where it operates as a load and generating unit in storage and sun and storage, respectively. Even though BSS acts as a voltage source, the behavior during the fault-on period is similar to that of grid-feeding inverters, i.e., current sources. According to Section 2.3.2, the short-circuit current of BSS, like in PV, is restricted to 1 pu. Henceforth, the active power profiles are similar to the corresponding (terminal) voltage profiles.

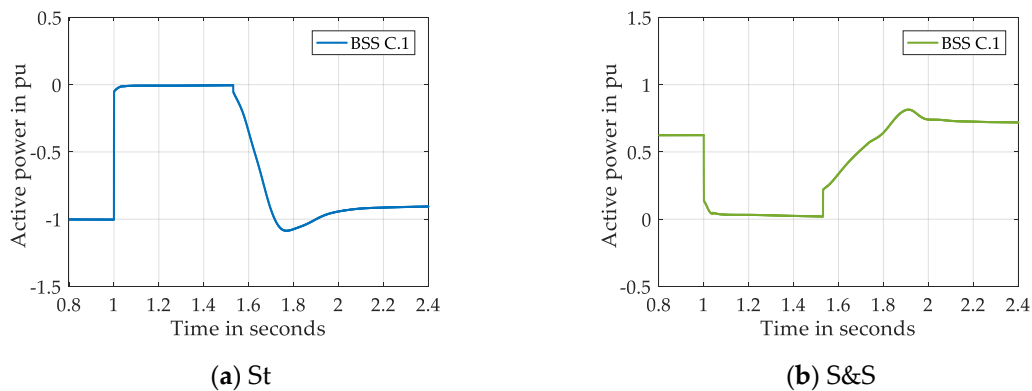


**Figure 24.** Real power of BSS of microgrid C (island mode) in: storage (a) and sun and storage (b) scenario.

## ii. Reactive Power

In Figure 25 the reactive power of the DGs in microgrid C is depicted. Due to the resistive-inductive (static and dynamic) loads, the DGs provide capacitive reactive power. Similar to the active power, the reactive power depends on the terminal voltage and output current of the DGs. Thus, the reactive power is relatively less during the fault-on period. After the fault clearance, the DGs close to the fault location act as inductive loads, since the corresponding terminal voltages are relatively less than the terminal voltages of the DGs that are relatively far away from the short-circuit location. Due to the disconnection of inductive motors, the power set-points of the DGs should be adjusted once the post-fault steady-state has been reached.

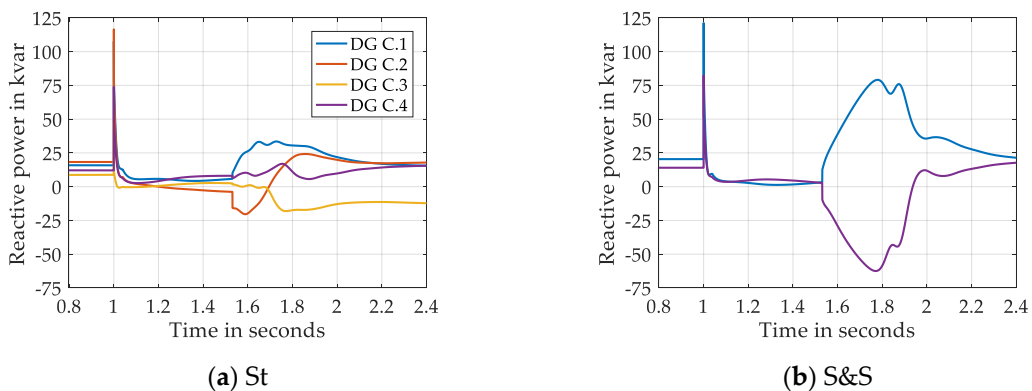


**Figure 25.** Reactive power of DGs of microgrid C (island mode) in: storage (a) and sun and storage (b) scenario.

The grid-feeding PV system—along with DGs and BSS—provides capacitive reactive power in the pre-fault period—see Figure 26. In contrast to the DGs, the reactive power of PV can be controlled during fault-on period. The output signals of the power control block (cf. Figure 3) along with the current limiter block are  $i_{d\_ref}$  and  $i_{q\_ref}$ . Due to the disconnection of induction motors 40 ms after the fault incident, the (inductive) reactive power demand in the microgrid is relatively not high during fault-on and especially post-fault period. Further, by giving 100% priority to active power (i.e., no reactive power provision) under short-circuit conditions, a positive effect on the transient stability has been noticed in [17]. Thus, the PV system is made to reduce its reactive power completely to zero.

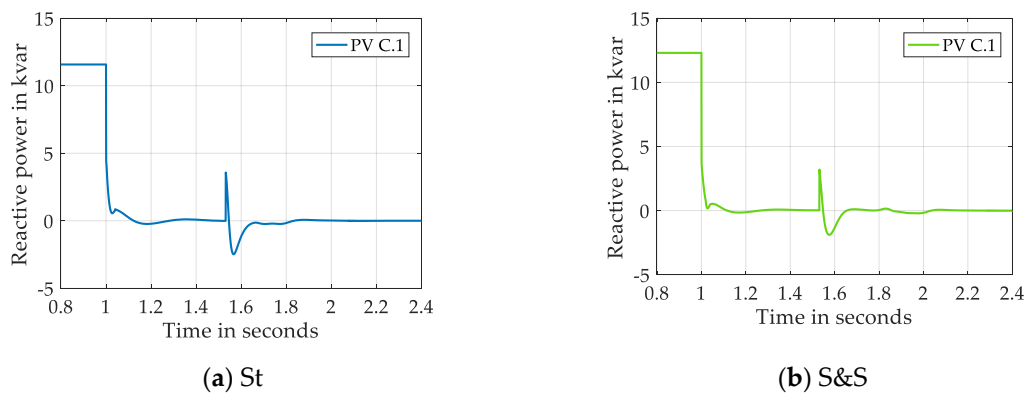


**Figure 26.** Reactive power of PV of microgrid C (island mode) in: storage (a) and sun and storage (b) scenario.

Similarly, the main input signals of the current control block in grid-forming BSS are (cf. Figure 7)  $i_{d\_v\_ref}$  and  $i_{q\_v\_ref}$ . In case of a short-circuit, modified very high reference current signals, i.e., the mentioned signals, will be fed into the current control block, such that  $i_{q\_v\_ref}$  is equal to zero. Hence, the grid-forming BSS acting now as a current source is forced not to provide any capacitive reactive power directly after the fault incident—see Figure 27. Since the BSS acts as a load in scenario “storage”, the capacitive reactive power is shown with a minus sign.

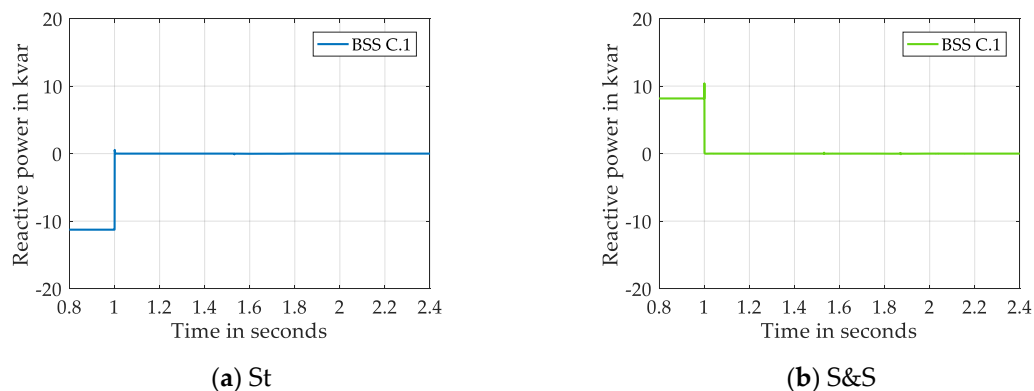


**Figure 27.** Reactive power of BSS of microgrid C (island mode) in: storage (a) and sun and storage (b) scenario.

### iii. Output Current

The initial and the sustained short-circuit currents of the DGs (cf. Figure 28) are within the acceptable limits [23]. DG C.3 in scenario “storage” is characterized with a relatively higher output current due to the closeness to the fault location.

In contrast to DGs, the output current of PV and BSS can be controlled by varying the input current signals of the current controller block. Otherwise, the power electronic components will be overloaded and/or damaged due to very high short-circuit currents. [35,43] The output current profile of the grid-feeding PV system is shown in Figure 29.

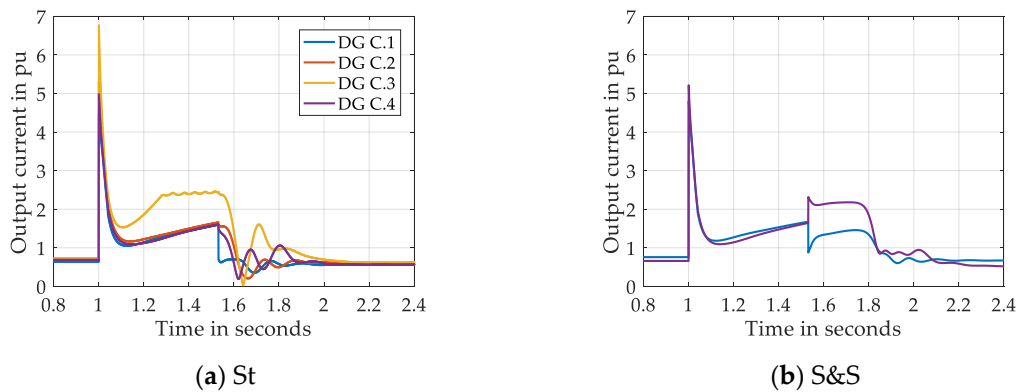


**Figure 28.** Current of DGs of microgrid C (island mode) in: storage (a) and sun and storage (b) scenario.

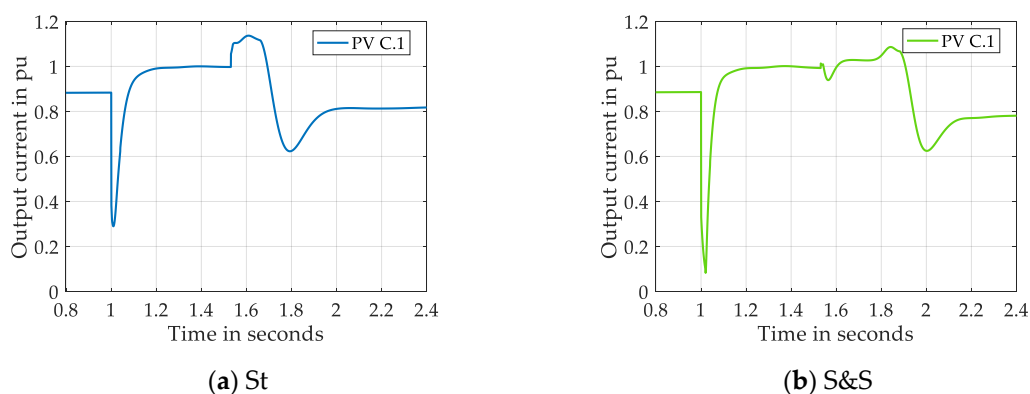


**Figure 29.** Current of PV of microgrid C (island mode) in: storage (a) and sun and storage (b) scenario.

Soon after the sudden voltage drop due to the fault, the difference between the DC currents  $I_{DC}$  and  $I_{PV}$  in PV (see Figure 3) becomes positive. As a result of the increase of  $I_C$ , the DC-link voltage  $V_{DC}$  rises. With the help of the DC voltage controller, the output current of PV is indirectly increased by increasing the equivalent (d-component) input signal of the current controller block. [17] At the same time,  $i_{q\_ref}$  is set to zero by giving entire priority to  $i_{d\_ref}$ . Due to the corresponding time constants in the control loops, it takes several milliseconds until the output current reaches 1 pu. Due to the reduction in the reactive power soon after the short-circuit occurrence, the post-fault (steady-state) current is different from the pre-fault current. However, the active power output remains unaltered (cf. Figure 23), since the solar irradiance and the module temperature were assumed to be constant in the transient stability analyses.

The BSS in microgrid C acts as a generating unit in scenario “sun & storage”. Since the DC side of the storage system was modelled by a constant DC voltage source in this research work, a sudden increase in the output current is noticed in the BSS (see Figure 30). Further, the post-fault current is strongly dependent on the terminal voltage. On the other hand, the output current of the BSS acting as a load in scenario “storage” is reduced, since the operating mode (charging/storing) of the BSS remains unchanged.

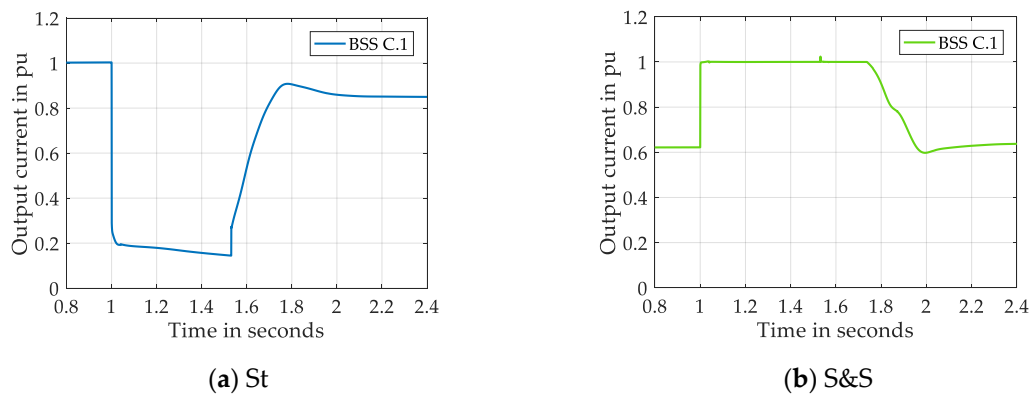


**Figure 30.** Current of BSS of microgrid C (island mode) in: storage (a) and sun and storage (b) scenario.

### 3.3. Effect of Pooling Microgrids on the System Stability

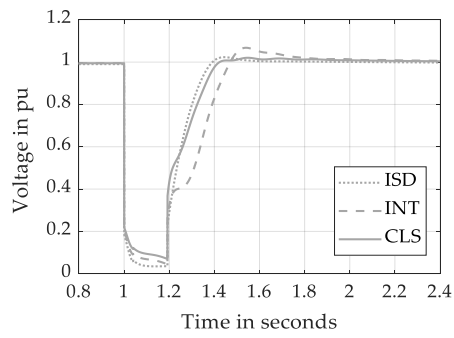
In this section, the simulation results of the three-phase short-circuit analysis on line L C.5 in microgrid C corresponding to the three operating modes (island, interconnection, and cluster) will be presented with respect to voltage, frequency and rotor angle stability. The studied fault was cleared after 192 ms, which corresponds to the minimum CCT among the scenarios and operating modes—classical scenario and interconnection mode.

#### 3.3.1. Voltage Stability

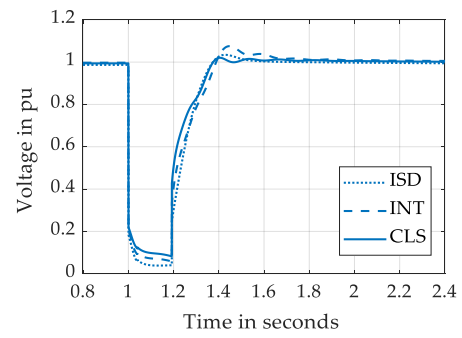
In Figure 31, the measured voltage on busbar C.5 in the different operating modes with respect to the five scenarios is illustrated. A positive effect on the minimum voltage during fault-on is noticed in the interconnected and clustered mode as against the islanded mode—*independent of the scenarios*. Except in scenario “night”, the clustered mode is characterized by a better voltage profile during fault-on and post-fault period. Even though the improvement in the voltage profiles of the scenarios between the fault incident and clearance is subtle, the influence on the frequency and rotor angle stability is significant in microgrids.

#### 3.3.2. Frequency Stability

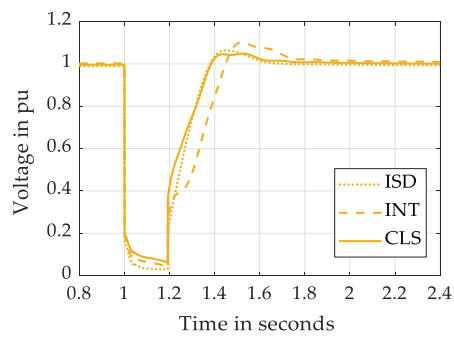
Due to space constraints, the frequency stability will be discussed taking the reference scenario, *i.e.*, classical, and the hybrid scenario (sun and storage) with the least number of DGs. Figure 32 shows the actual rotor angular frequency of the DGs in the three different operating modes. Similar to the voltage stability, the coupling of microgrids leads to an improvement in the frequency stability. Further, a positive impact is noticed also in the other scenarios, which are not shown in this research paper. Due to the disconnection of the induction motors after the fault occurrence, the post-fault steady-state value of the angular frequency of the DGs is not exactly equal to 1 pu. Further, secondary frequency control is not implemented in the microgrids, since the focus of this research work lies on the short-term stability analysis.



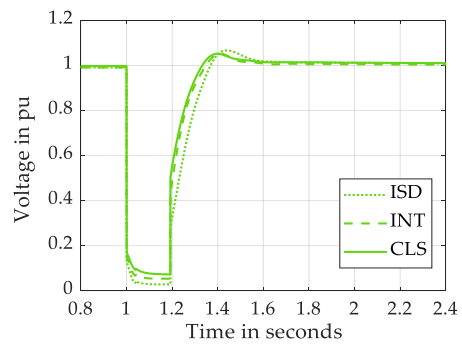
(a) CI



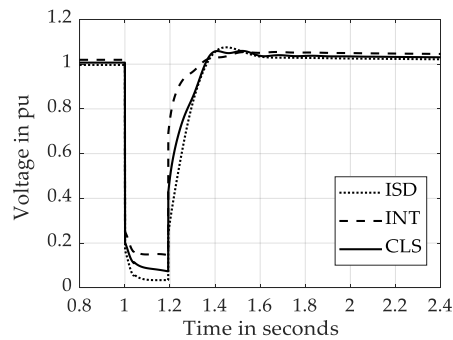
(b) St



(c) Su



(d) S&S



(e) Ni

**Figure 31.** Voltage on busbar C.5 in the islanded, interconnected and clustered mode in: classical (a), storage (b), sun (c), sun and storage (d) and night (e) scenario.

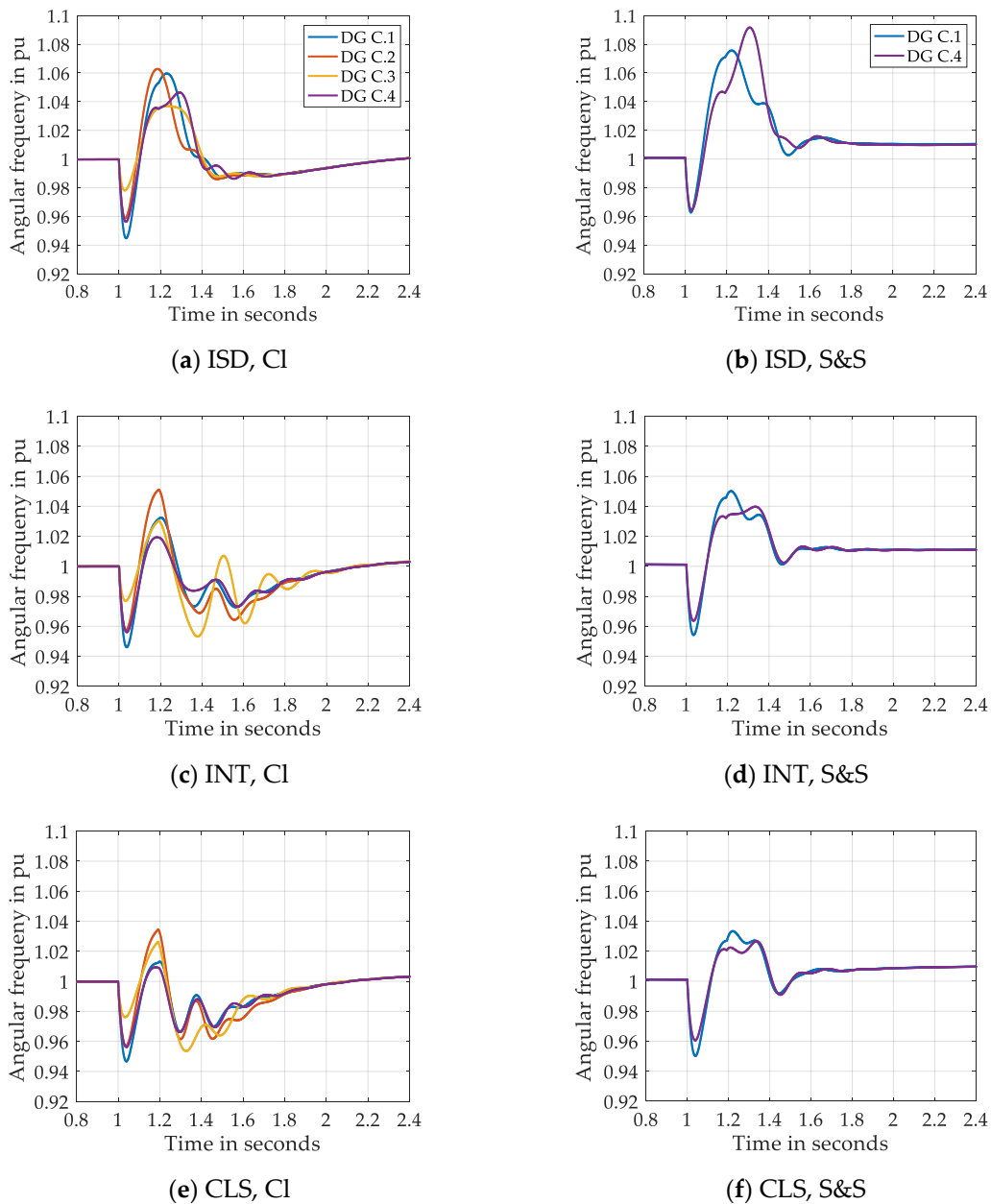


**Figure 32.** Actual rotor angular frequency of the DGs in the isolated, interconnected and clustered mode in: classical (a,c,e) and sun and storage (b,d,f) scenario.

### 3.3.3. Rotor Angle Stability

The rotor angle (in the COI frame) of the DGs belonging to microgrid C in the three operating modes and scenario “classical” and “sun & storage” is presented in Figure 33. Regarding the classical scenario, the rotor angle oscillations (excursions) increase in coupled microgrids as against the isolated operating mode, thus a negative impact on the rotor angle stability. However, a marginal positive effect is observed in scenario “sun & storage”, which can be also noticed in the positive  $\Delta CCT$ —see Section 3.1.2. According to Figures 12 and 13 as well as the profiles of the other hybrid scenarios, rotor angle stability is deteriorated by coupling microgrids, like in the classical scenario.

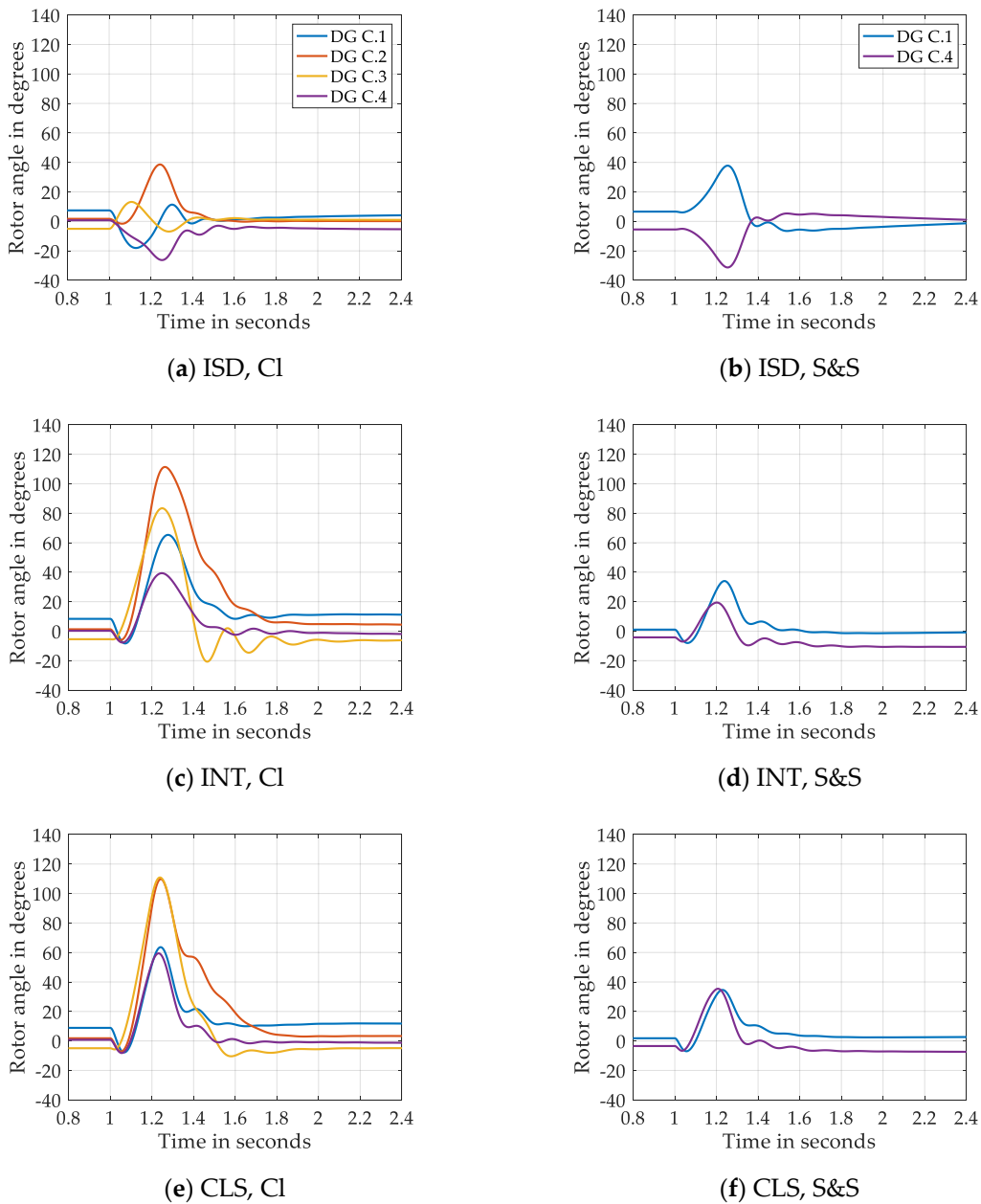


**Figure 33.** Relative rotor angle of the DGs in the islanded, interconnected and clustered mode in: classical (a,c,e), and sun and storage (b,d,f) scenario.

Based on the three types of system stability—for the fault on L C.5—optimal scenarios and operating modes can be selected (see Table 10) in the grid planning and/or during near real-time grid operation. The qualitative assessment with respect to the voltage stability was performed by analyzing the voltage drop soon after the fault incident as well as the post-fault voltage recovery. The frequency and the rotor angle stability were assessed qualitatively by studying the excursions and oscillations during fault-on and post-fault period. As against the hybrid scenarios, the scenario “classical” does not outperform in the investigated cases.

**Table 10.** Overview of the optimal scenarios in the different operating modes.

		CI	St (12 pm)	Su (2 pm)	S&S (3 pm)	Ni (8 pm)
Island	V		✓	✓		✓
	f			✓		✓
	$\delta$		✓	✓		✓
Interconnection	V		✓		✓	✓
	f			✓	✓	✓
	$\delta$		✓		✓	✓
Cluster	V		✓		✓	✓
	f			✓	✓	✓
	$\delta$				✓	✓

According to the qualitative rotor angle stability analysis (highlighted in Table 10), it can be concluded that:

- Storage, sun and night scenario can be chosen in the **islanded** operation of microgrid C.
- Furthermore, storage, sun and storage, and night scenario outperform the other scenarios in the **interconnected** operating mode.
- In the **clustered** operating mode, sun and storage, and night scenario are beneficial.

Scenario “night” is the most optimal scenario in each operating mode with respect to the system stability, whereas scenario “classical” is not advantageous. In practice, it is significantly tedious to draw conclusions taking every fault location and every microgrid topology into account. Hence, the selection of the optimal scenarios and operating modes should be performed by considering only the critical fault(s). Nevertheless, the decision-making process based on the qualitative stability assessment leads to general conclusions with respect to numerous scenarios and operating modes as well as different topologies in a relatively larger cluster environment.

### 3.4. System Stability Degree in Operating Modes and Scenarios

#### 3.4.1. Operating Modes

The values of the SSD for the corresponding fault clearing time—calculated using the micro-hybrid method according to Equation (8)—have been plotted for the different cases (13 out of 15) in Figure 34. The minimum fault clearing time of 60 ms has been highlighted by a vertical dashed line. It has been discussed in Section 2.6 that an SSD of 10% was chosen as the threshold value for determining CCCT, which has been also shown in the form of a horizontal dashed line. It should be noted that the stability reserve degree and the participation factor of individual synchronous generators will be analyzed in the upcoming research work. However, the corresponding analysis taking the classical scenario into account can be found in [20].

If the fault is cleared 1 ms (impossible in practice) after the fault occurrence, the SSD lies around 100%. If the fault clearance is increased, the system stability reserve drops. The system can be characterized as uncritical (or the fault can be considered as severe) in case of a low value of the gradient of the SSD profile. Profiles with a very high slope are classified to be critical, since the SSD value gets reduced significantly. Any delay in clearing the fault can lead to instability. It can be inferred from Figure 34a that the profile in the islanded mode is less critical than that in the interconnected and clustered mode. Furthermore, the difference between the CCT and CCCT values lies between 35% and 45%.

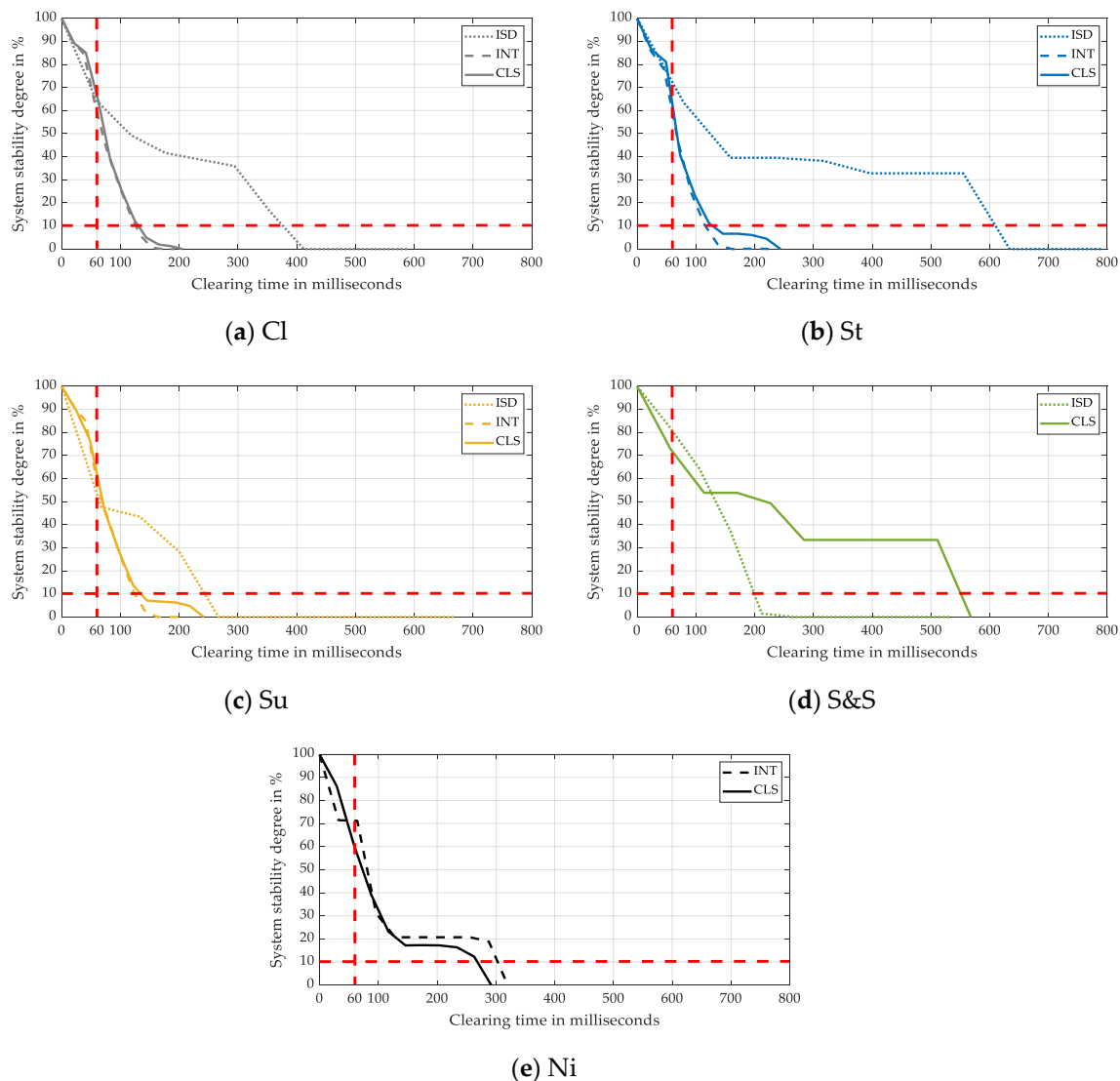


**Figure 34.** System stability degree versus fault clearing times regarding the different operating modes in: classical (a), storage (b), sun (c), sun and storage (d), and night (e) scenario.

The SSD profile of the hybrid scenarios is illustrated in Figure 34b–e. The profiles in the coupled modes are similar as against the islanded mode. The interconnected and islanded mode in scenarios “sun & storage” and “night” have been purposefully not shown in the figure, since the SSD—in these two cases—based on the performed TDS were not plausible. A detailed analysis of these two profiles was not performed in this research work. Further, the SSD of several cases (5 out of 13), e.g., scenario “sun” in the islanded mode, lies around 0% for a clearing time less than the CCT. The corresponding clearing times up to the CCT were not plausible. Hence, the values of the SSD were assumed to be zero. These profiles should be further investigated.

In general, the islanded mode, independent of the scenarios, is characterized by the best SSD profile—in terms of the CCT, the CCCT and the slope of SSD profiles. The profiles in interconnection and in cluster mode are acceptable. However, the sensitivity of the SSD for various clearing times is relatively high. The trend (slope) of the SSD profiles should be analyzed in case of scenarios and operating modes with higher CCT values.

The corrected critical clearing time (CCCT) can be determined based on the set threshold value in the SSD profiles, i.e., 10% SSD. Table 11 lists the CCT, CCCT, and their difference  $\Delta CCT$  in the investigated cases. CCCT values less than 60 ms are not noticed in any of the cases. It is recommended

to adjust the settings of protection systems based on the *CCCT*, instead of the *CCT*, so that the risk of system losing stability can be reduced further.

**Table 11.** Overview of the *CCT*, *CCCT*, and  $\Delta$ *CCT* in the three operating modes with respect to the five scenarios.

		<i>CCT</i> in ms	<i>CCCT</i> in ms	$\Delta$ <i>CCT</i>
Classical	ISD	588	377	36%
	INT	192	126	34%
	CLS	206	131	36%
Storage	ISD	793	610	23%
	INT	230	116	50%
	CLS	244	129	47%
Sun	ISD	667	243	64%
	INT	205	124	40%
	CLS	242	135	44%
Sun & Storage	ISD	531	200	62%
	INT	568	-	-
	CLS	571	552	3%
Night	ISD	1058	-	-
	INT	321	303	6%
	CLS	292	269	8%

### 3.4.2. Scenarios

In case of analyzing the SSD regarding the scenarios in the different operating modes, the profiles depicted in Figure 35 can be taken into consideration. Similar to the previous section, the sensitivity or the slope of the SSD profiles should be taken into account while selecting the optimal scenario in each operating mode. The scenario with the highest value of *CCT* in each operating mode is characterized by the best SSD profile. The magnitude of the slope of the profiles corresponds to the respective *CCT* value. If the (differential) protection system is supposed to clear a fault in cluster mode after, e.g., 100 ms, scenario “sun & storage” can be preferred as the optimal scenario. On the other hand, the *CCCT* values determined based on the SSD’s threshold value are listed in Table 12.

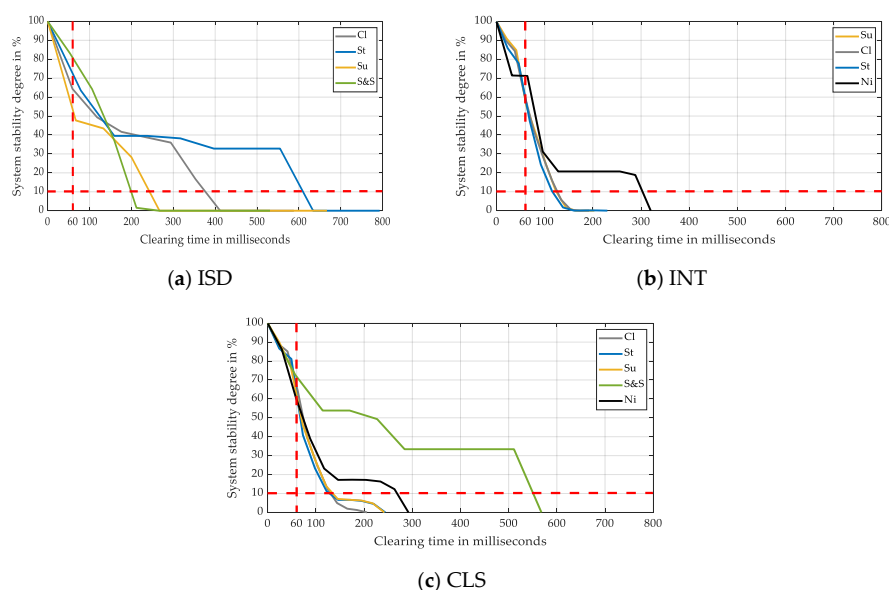


**Figure 35.** System stability degree versus fault clearing times regarding the different scenarios in: island (a), interconnection (b), and cluster (c) mode.

**Table 12.** Overview of the  $CCT$ ,  $CCCT$ , and  $\Delta CCT$  in the five scenarios with respect to the three operating modes.

		$CCT$ in ms	$CCCT$ in ms	$\Delta CCT$
<b>Island</b>	<b>Cl</b>	588	377	36%
	<b>St</b>	793	610	23%
	<b>Su</b>	667	243	64%
	<b>S&amp;S</b>	531	200	62%
	<b>Ni</b>	1058	-	-
<b>Interconnection</b>	<b>Cl</b>	192	126	34%
	<b>St</b>	230	116	50%
	<b>Su</b>	205	124	40%
	<b>S&amp;S</b>	568	-	-
	<b>Ni</b>	321	303	6%
<b>Cluster</b>	<b>Cl</b>	206	131	36%
	<b>St</b>	244	129	47%
	<b>Su</b>	242	135	44%
	<b>S&amp;S</b>	571	552	3%
	<b>Ni</b>	292	269	8%

### 3.5. Comparison of Critical Energy in Scenarios and Operating Modes

In this section, the critical energy of the system and of the critical machine will be compared with each other—considering the islanded and clustered operating modes—in order to analyze the ratio of the critical energies. The calculation of the SSD is based on the system critical energy. According to the classical scenario—cf. Figure 17a—and other hybrid scenarios corresponding to the respective  $CCT$ , the critical DG can be generally easily noticed. Unlike in large transmission systems, a distinct formation of a critical group of DGs, approaching the stability limit, has been not observed in the microgrids, which has been also given in [19,20].

#### 3.5.1. Island

Figure 36 shows the absolute value of  $E_{cr}$  and  $E_{cr\_cm}$  as well as their ratio in each scenario for the fault on L C.5. Further, the  $CCT$  of the scenarios has been illustrated. The system critical energy decreases with a reduction in the number of the operating DGs (cf. Table 3). The trend of the profile of  $E_{cr\_cm}$  in the scenarios cannot be compared with that of  $E_{cr}$ . The ratio of  $E_{cr\_cm}$  and  $E_{cr}$  is between ca. 20% and 60%, where the scenarios with fewer numbers of DGs are characterized by a higher ratio. A direct correlation between the critical energies and  $CCT$  values cannot be found in this research work, which will be analyzed in Section 3.6.

#### 3.5.2. Cluster

The critical energies and the  $CCT$  in the clustered mode are depicted in Figure 37. Similar to the islanded mode, the share of  $E_{cr\_cm}$  in  $E_{cr}$  in the clustered (and also interconnected) operating mode lies between about 20% and 50%. Further, a direct proportionality between  $E_{cr}$  and the number of DGs can be seen. However, the absolute values of  $E_{cr}$  and  $E_{cr\_cm}$  differ significantly as against the values in the islanded mode.

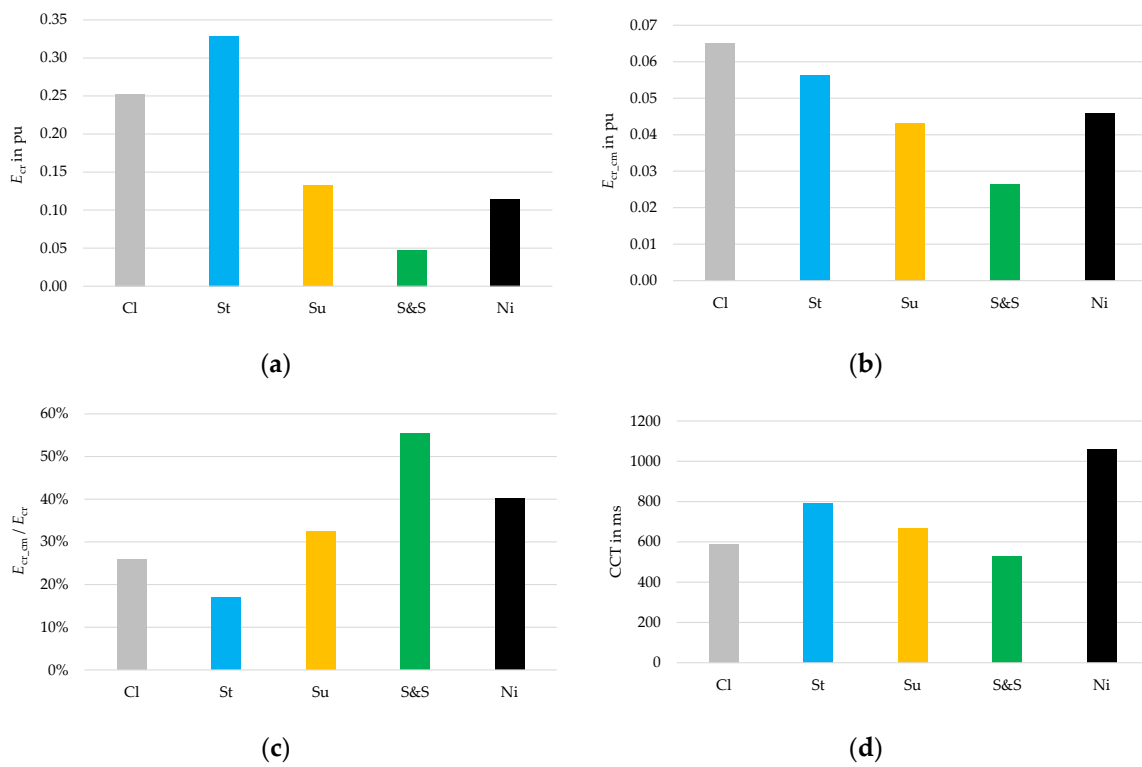


**Figure 36.** Analysis of the critical energies in the islanded mode: system critical energy (a), critical energy of the critical machine (b), ratio of the critical energies (c), and CCT (d).

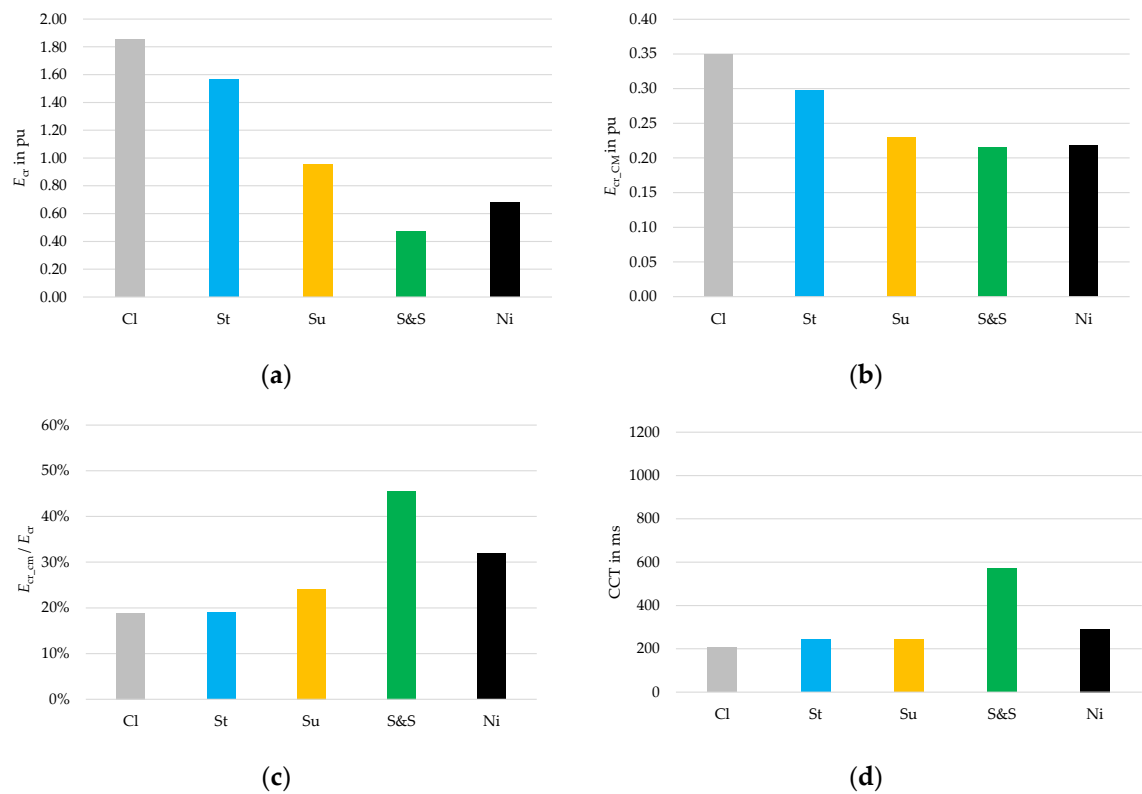


**Figure 37.** Analysis of the critical energies in the clustered mode: system critical energy (a), critical energy of the critical machine (b), ratio of the critical energies (c), and CCT (d).

### 3.6. Influence of Fault Location on Critical Energy in Cluster Mode

The three-phase fault on both ends of L C.5, i.e., very close to BB C.5 and BB C.6, was studied to determine a correlation between the  $CCT$  and the critical energy of the system and of the critical machine. The critical generator in each scenario in the clustered operating mode is DG C.2, whereas DG C.1 represents the critical machine in scenario “sun & storage”. It should be noted that the scenarios will not be compared with each other in this section. However, the  $CCT$ ,  $E_{cr}$ , and  $E_{cr\_cm}$  will be analysed in each scenario—cf. Figure 38.

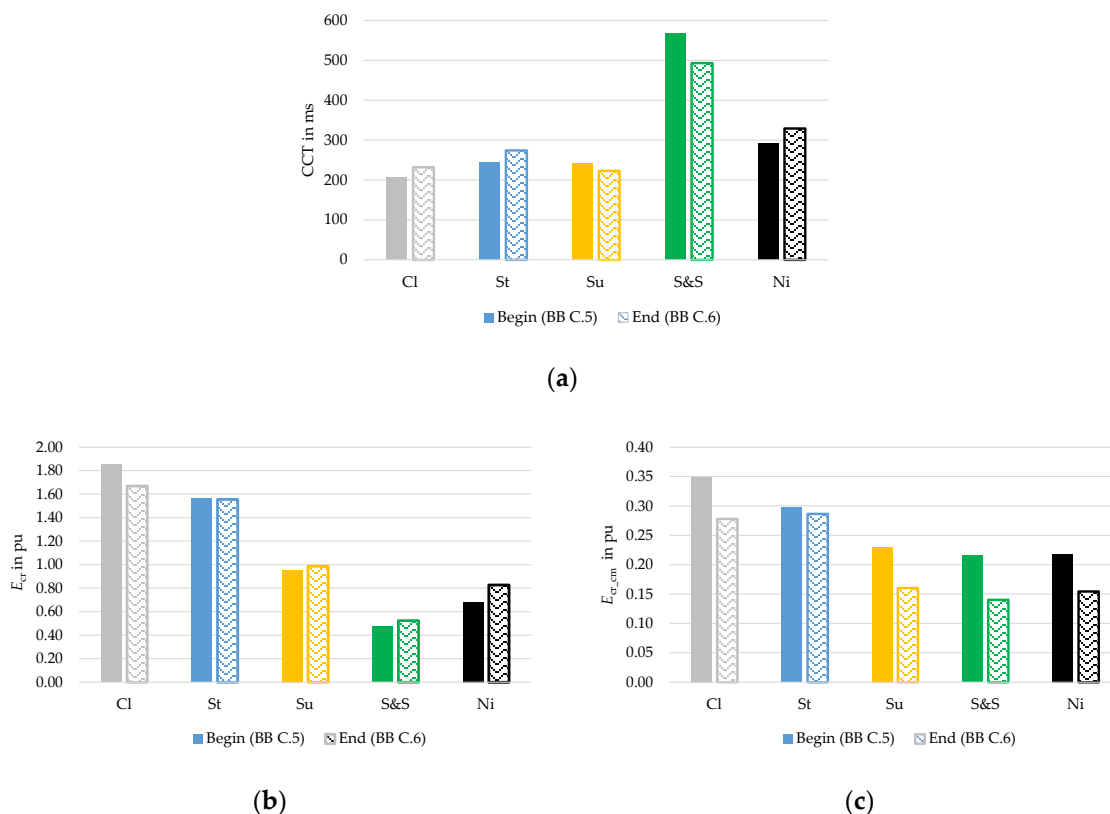


**Figure 38.** Minimum allowable clearing time and critical energy in each scenario:  $CCT$  (a), system critical energy (b) and critical energy of the critical machine (c).

In a one-machine infinite bus system, an inverse proportionality exists between the  $CCT$  and critical energy of the machine, modelled as a classical 2nd order generator. In case of a three-phase fault very close to the synchronous generator, the terminal voltage is almost zero during fault-on. The resulting change in the KE and corresponding PE is relatively higher than that of a case (with the identical pre-fault operating point) with an insignificant drop in the terminal voltage—like in a single-phase fault. The  $CCT$  of the critical fault is less as against the  $CCT$  of the fault with a residual voltage during fault-on period.

As against the short-circuit close to BB C.5, the fault next to BB C.6 corresponds to a relatively higher residual terminal voltage of the critical machine DG C.2 (see Figure 9, however in the clustered mode) in every scenario, except in scenario “sun & storage”. According to Figure 38, it can be inferred that the  $CCT$  values and critical energies are both directly and inversely proportional. In scenarios “classical”, “storage”, and “night”, an increase in the  $CCT$  is observed. This corresponds to an indirect proportionality with  $E_{cr\_cm}$ , like in the above mentioned one-machine infinite bus system. However, a negative difference of the  $CCT$  is related to a negative difference of  $E_{cr\_cm}$  in scenarios “sun” and “sun & storage” (critical machine being DG C.1).

In principle, finding a direct correlation between the *CCT* and the system critical energy with respect to different fault locations, especially in the clustered operating mode, can be misleading. In the future research work, the correlation between the *CCT* and energies should be investigated in detail. For example, by analyzing the *CCT* (of critical faults) and the critical energy of every DG or group of “critical” DGs in the microgrids, the steady-state operating point of DGs can be adjusted.

## 4. Summary and Outlook

### 4.1. Summary

Pooling nearby off-grid hybrid microgrids—comprising diesel engine-driven synchronous generators as well as grid-feeding photovoltaics (PV) and grid-forming battery storage systems (BSS)—leads to a reduction in the fuel costs and greenhouse gas emissions as well as to an increase in the security of supply. In the planning phase and in near real-time operation, coupling of microgrids should be investigated not only in the steady-state, but also from the transient stability point of view: both qualitatively and quantitatively. This calls for a detailed dynamic microgrid modelling and three-phase short-circuit analysis. Using the recently developed micro-hybrid method—combining time-domain simulations and transient energy function analyses—quantitative transient stability assessment can be performed.

Hence, three spatially close realistic off-grid microgrids (A, B, and C) were modelled and analyzed in the framework of this research regarding three operating modes (island “C”, interconnection “A and B”, and cluster “A, B, and C”) as well as five scenarios with respect to different instants of time on a partly sunny day. Scenario “classical” represents microgrids with diesel generators (DGs) only, whereas hybrid scenarios “storage”, “sun”, “sun & storage”, and “night” correspond to microgrids with DGs, PV, and BSS (either as loads or as generation units).

Firstly, critical clearing time (CCT) profiles of the microgrids were compared considering 15 cases, by categorizing three operating modes and five scenarios. Secondly, qualitative stability assessment was performed in microgrid C (island mode) for a (critical) short-circuit location very close to a DG and a BSS. The fault behavior of the hybrid microgrids was verified at the system and the equipment level, and was also compared with the response of the classical microgrid. Thirdly, the effect of different operating modes of microgrids was studied among the scenarios from the system stability—i.e., voltage, frequency, and rotor angle stability—point of view. In the last two sections, transient stability was accessed quantitatively with the help of the micro-hybrid method. Regarding the studied fault location in microgrid C, a system stability degree (SSD) was calculated for each fault clearing time in the operating modes and scenarios. Further, the critical energy of the system and the critical machine as well as the effect of the fault location on the critical energy were investigated among scenarios and operating modes.

The key findings of this research work can be summed up as follows:

- **Critical clearing times:** According to the *CCT* profiles of the microgrids (based on the risk level) with respect to the operating modes and scenarios, it can be concluded that, any scenario can be preferred in the islanded mode. However, scenario “sun & storage” is characterized by better *CCT* profiles in the interconnected and clustered mode. In general, coupling classical or hybrid microgrids is not critical with respect to the *CCT* values for the considered high load operating point on a partly sunny day. However, interconnection and cluster mode are characterized by a relatively higher risk of transient stability as against the island mode.
- **Fault behavior of microgrid C in island mode:** The response of microgrid C—in the pre-fault, fault-on and post-fault period—at both system and equipment level for the simulated short-circuit can be assessed as plausible and thereby the dynamic system modelling can be validated.
- **Effect of pooling microgrids on the system stability:** Scenarios “storage”, “sun”, and “night” of microgrid C perform better in the islanded operation regarding the critical short-circuit location. On the other hand, scenarios “storage”, “sun & storage”, and “night” outperform in the

interconnected mode. Further, scenarios “sun & storage” and “night” have a positive impact on the system stability in the clustered mode. In this studied case, scenario “night” can be categorized to be the most optimal in each operating mode, whereas scenario “classical” does not perform better among the scenarios. Analyses regarding the selection of the optimal operating modes and scenarios should be executed on a regular basis—by considering only the critical fault(s) with respect to either location or *CCT* values—in the near real-time grid operation.

- **System stability degree in operating modes and scenarios:** The SSD was determined for each corresponding (stable) fault clearing time in various cases with the help of the micro-hybrid method. The SSD profile of the scenarios in interconnection and cluster mode is, in terms of the severity of the fault and sensitivity of the system, more critical than that in island mode, which is characterized by the slope of the profiles. The relative difference between the *CCT* and the corrected critical clearing time (*CCCT*) of the cases, calculated based on the threshold value of the SSD, lies between 3% and 64%. It is recommended to take *CCCT* into account while setting the protection systems in microgrids, so that the risk of system losing stability can be reduced even further. In addition, the gradient of the SSD profiles should be considered while selecting the optimal scenario in the operating modes and scenarios.
- **Comparison of critical energy in scenarios and operating modes:** According to the analyses of the absolute value of the critical energy of the system and of the critical machine as well as the *CCT* (of the studied fault in different scenarios and operating modes), it can be inferred that, the ratio of the critical energy of the critical machine to that of the system lies between 20% and 60%. The ratio is relatively higher in the scenarios with a smaller number of active DGs.
- **Influence of fault location on critical energy in cluster mode:** In case of a one-machine infinite bus system, an inverse proportionality between the *CCT* and critical energy of the machine (simplified 2nd order model) can be observed. Further, the ratio of the *CCT* of the critical fault to the *CCT* of the fault with a residual voltage during fault-on period is relatively high. It can be concluded from the simulation results (of two nearby fault locations) that the *CCT* and critical energy values of the critical machine are both directly and inversely proportional. Finding a direct correlation between the *CCT* and the critical energy of the system with respect to different fault locations, especially in cluster mode, can be misleading. However, investigation of the *CCT* of critical faults as well as the critical energy of every DG or a group of “critical” DGs can help to set optimal steady-state operating points of DGs—in the grid planning phase or in the near real-time operation.

All in all, the following conclusions can be drawn:

- Coupling classical or hybrid microgrids is, in principle, technically feasible regarding *CCT*. However, interconnection and cluster mode exhibit a relatively higher risk of transient stability as against the island mode.
- The hybrid scenarios have a more positive effect on the system stability than scenario “classical”. Furthermore, scenario “night” (DGs and BSS) can be ranked as the most optimal in each operating mode, while scenario “classical” (DGs only) has an overall negative effect compared to the other scenarios.
- According to the quantitative TSA, the profiles of SSD versus clearing times of the scenarios in island mode are better than the SSD profiles in interconnection and cluster mode—with respect to the *CCT*, the *CCCT*, and the slope of SSD profiles. In spite of the relatively higher gradient, the SSD profiles in the coupled modes are also acceptable.
- Further, according to the results regarding the effect of the fault location on the critical energy, there exists a direct and indirect proportionality between the *CCT* and critical energy values of the critical machine.

## 4.2. Outlook

In the framework of this research, three off-grid microgrids were studied taking five scenarios and three operating modes into account. In case of a cluster of more than three microgrids, apart from ring topology, different coupling possibilities should be analyzed—from system stability point of view, especially large-signal rotor angle stability—in order to choose optimal operating modes and scenarios.

With respect to the modelling of microgrids in, e.g., agriculture-dominated rural areas, the share of DGs can be reduced not only by further increasing the installed capacity of PV and BSS, but also by installing eco-friendly biogas generators and micro hydropower plants. Due to different injection delay times—of the mentioned synchronous generators—in case of disturbances, and consequently different courses of the forward and the backswing of the generators, random rotor swings can be observed. This calls for a detailed qualitative and especially quantitative TSA of such hybrid microgrids in different operating modes.

In hybrid microgrids with a significant share of inverter-based systems, PV and BSS should be modelled using EMT models instead of RMS models. Due to the recent developments in grid modelling and simulation tools [57], co-simulation (RMS and EMT) of microgrids can be performed.

As a result of the extension of power transmission networks—in developing and under-developed countries—with long-term projects connecting remote areas, alongside decentralization, future interconnected stand-alone hybrid microgrids can be operated not only in the islanded mode, but also by connecting to the main transmission and distribution grids. Hence, the dynamic behavior as well as the qualitative and quantitative operational limits of such coupled—off-grid and grid-connected—microgrids with different topologies should be determined in the planning phase and also in near real-time grid operation. Further, switching operations and measures to improve the dynamic stability and security of hybrid microgrids can be investigated in detail.

**Author Contributions:** Conceptualization, K.V.; methodology, K.V. and H.A.; software, H.A.; validation, K.V. and H.A.; formal analysis, H.A. and K.V.; investigation, H.A.; data curation, K.V.; writing—original draft preparation, K.V.; writing—review and editing, K.V., H.A., and M.L.; visualization, H.A. and K.V.; supervision, K.V. All authors have read and agreed to the published version of the manuscript.

**Funding:** This research received no external funding.

**Conflicts of Interest:** The authors declare no conflicts of interest.

## References

1. International Renewable Energy Agency (IRENA). Off-Grid Renewable Energy Systems: Status and Methodological Issues. Available online: [https://www.irena.org/-/media/Files/IRENA/Agency/Publication/2015/IRENA\\_Off-grid\\_Renewable\\_Systems\\_WP\\_2015.pdf](https://www.irena.org/-/media/Files/IRENA/Agency/Publication/2015/IRENA_Off-grid_Renewable_Systems_WP_2015.pdf) (accessed on 13 January 2020).
2. Carnegie Mellon University (CMU). Available online: <https://www.cmu.edu/ceic/assets/docs/publications/reports/2014/micro-grids-rural-electrification-critical-rev-best-practice.pdf> (accessed on 13 January 2020).
3. Motoren- und Turbinen-Union (MTU). Available online: <https://www.mtu-solutions.com/en/en/stories/power-generation/gas-generator-sets/microgrid-cooperation-with-qinous.html> (accessed on 13 January 2020).
4. Caterpillar. Available online: [https://www.cat.com/en\\_US/by-industry/electric-power-generation/Articles/White-papers/white-paper-hybrid-microgrids-the-time-is-now.html](https://www.cat.com/en_US/by-industry/electric-power-generation/Articles/White-papers/white-paper-hybrid-microgrids-the-time-is-now.html) (accessed on 13 January 2020).
5. United Nations (UN). Available online: <https://sustainabledevelopment.un.org/content/documents/interconnections.pdf> (accessed on 13 January 2020).
6. Microgrid Knowledge. Available online: <https://microgridknowledge.com/bronzeville-microgrid-cluster/> (accessed on 13 January 2020).
7. Ejal, A.A.; Yazdavar, A.H.; El-Saadany, E.F.; Ponnambalam, K. On the Loadability and Voltage Stability of Islanded AC–DC Hybrid Microgrids During Contingencies. *IEEE Syst. J.* **2019**, *13*, 4248–4259. [CrossRef]
8. Saleh, M.S.; Althaibani, A.; Esa, Y.; Mhandi, Y.; Mohamed, A. Impact of Clustering Microgrids on Their Stability and Resilience during Blackouts. In Proceedings of the International Conference on Smart Grid and Clean Energy Technologies, Offenburg, Germany, 20–23 October 2015; pp. 195–200.

9. Shafiee, Q.; Dragicevic, T.; Vasquez, J.C.; Guerrero, J.M. Hierarchical Control for Multiple DC-Microgrids Clusters. *IEEE Trans. Energy Convers.* **2014**, *29*, 922–933. [[CrossRef](#)]
10. Shafiee, Q.; Dragicevic, T.; Vasquez, J.C.; Guerrero, J.M. Modeling, Stability Analysis and Active Stabilization of Multiple DC-Microgrid Clusters. In Proceedings of the ENERGYCON, Dubrovnik, Croatia, 13–16 May 2014; pp. 1284–1290.
11. Nikolakakos, I.P.; Zeineldin, H.H.; El-Moursi, M.S.; Hatziargyriou, N.D. Stability Evaluation of Interconnected Multi-Inverter Microgrids through Critical Clusters. *IEEE Trans. Power Syst.* **2016**, *31*, 3060–3072. [[CrossRef](#)]
12. Zhao, Z.; Yang, P.; Wang, Y.; Xu, Z.; Guerrero, J.M. Dynamic Characteristics Analysis and Stabilization of PV-Based Multiple Microgrid Clusters. *IEEE Trans. Smart Grid* **2017**, *10*, 805–818. [[CrossRef](#)]
13. He, J.; Wu, X.; Wu, X.; Xu, Y.; Guerrero, J.M. Small-Signal Stability Analysis and Optimal Parameters Design of Microgrid Clusters. *IEEE Access* **2019**, *7*, 36896–36909. [[CrossRef](#)]
14. Majumder, R. Some aspects of stability in microgrids. *IEEE Trans. Power Syst.* **2013**, *28*, 3243–3252. [[CrossRef](#)]
15. Pavella, M.; Ernst, D.; Ruiz-Vega, D. *Transient Stability of Power Systems: A Unified Approach to Assessment and Control*; Kulwer: Norwell, MA, USA, 2000.
16. CIGRE. Available online: <https://e-cigre.org/publication/325-review-of-on-line-dynamic-security-assessment-tools-and-techniques> (accessed on 13 January 2020).
17. Veerashekar, K.; Bichlmaier, A.; Luther, M. Transient stability of hybrid stand-alone microgrids considering the DC-side of photovoltaics. In Proceedings of the 4th International Hybrid Power Systems Workshop, Crete, Greece, 22–23 May 2019; pp. 1–10.
18. Veerashekar, K.; Eichner, S.; Luther, M. Modelling and transient stability analysis of interconnected autonomous hybrid microgrids. In Proceedings of the 13th IEEE PES PowerTech Conference, Milan, Italy, 23–27 June 2019; pp. 1–6.
19. Veerashekar, K.; Schuehlein, P.; Luther, M. Quantitative transient stability assessment in microgrids combining both time-domain simulations and energy function analysis. *Int. J. Electr. Power Energy Syst.* **2020**, *115*, 1–12. [[CrossRef](#)]
20. Veerashekar, K.; Flick, M.; Luther, M. The micro-hybrid method to assess transient stability quantitatively in pooled off-grid microgrids. *Int. J. Electr. Power Energy Syst.* **2020**, *117*, 1–12. [[CrossRef](#)]
21. Veerashekar, K.; Flick, M.; Luther, M. Small-signal stability of interconnected autonomous microgrids (German: Kleinsignalstabilität von vernetzten autonomen Mikronetzen). In Proceedings of the International ETG Congress, Esslingen am Neckar, Germany, 8–9 May 2019; pp. 387–392.
22. Machowski, J.; Bialek, J.W.; Bumby, J.R. *Power System Dynamics: Stability and Control*, 2nd ed.; Wiley: Chichester, UK, 2012.
23. German Generator GmbH. Available online: <https://germangenerator.com/products/industrial-power-generators/> (accessed on 15 January 2020).
24. Sharp. Available online: <https://www.sharp.de/cps/rde/xchg/de/hs.xsl/-/html/product-details-solar-modules.htm?product=NQR258H> (accessed on 15 January 2020).
25. SMA Solar Technology. Available online: <https://www.sma.de/en/products/solarinverters/sunny-tripower-60.html> (accessed on 16 January 2020).
26. SMA Solar Technology. Available online: <https://www.sma.de/en/products/solarinverters/sunny-tripower-core1.html> (accessed on 16 January 2020).
27. IEEE PES. Available online: [https://resourcecenter.ieee-pes.org/technical-publications/technical-reports/PES\\_TR0066\\_062018.html](https://resourcecenter.ieee-pes.org/technical-publications/technical-reports/PES_TR0066_062018.html) (accessed on 16 January 2020).
28. Stenzel, D.; Hewes, D.; Viernstein, L.; Würfl, T.; Witzmann, R. Investigation of demand trends and their impacts on stationary and dynamic aggregated load behaviour. In Proceedings of the International ETG Congress, Esslingen am Neckar, Germany, 8–9 May 2019; pp. 171–176.
29. DiGSILENT/PowerFactory. *Technical Reference Documentation—Asynchronous Machines*; DiGSILENT/PowerFactory: Gomarigen, Germany, 2017; pp. 1–36.
30. Engineers Edge. Available online: [https://www.engineersedge.com/motors/classification\\_electric\\_motors\\_13882.htm](https://www.engineersedge.com/motors/classification_electric_motors_13882.htm) (accessed on 17 January 2020).
31. University of Oviedo. Available online: [http://ocw.uniovi.es/pluginfile.php/5424/mod\\_resource/content/1/Guia%20de%20General%20Electric%20motores%20I.pdf](http://ocw.uniovi.es/pluginfile.php/5424/mod_resource/content/1/Guia%20de%20General%20Electric%20motores%20I.pdf) (accessed on 17 January 2020).

32. FG Wilson. Available online: <http://www.fgwilson.ie/files/generator-set-iso8528-5-2005-operating-limits.pdf> (accessed on 17 January 2020).
33. International Organization for Standardization (ISO). *ISO 8528-5:2013—Reciprocating Internal Combustion Engine Driven Alternating Current Generating Sets—Part 5: Generating Sets*; ISO: Geneva, Switzerland, 2013.
34. Kroutikova, N.; Hernandez-Aramburo, C.A.; Green, T.C. State-space model of grid-connected inverters under current control mode. *IET Electr. Power Appl.* **2007**, *1*, 329–338. [[CrossRef](#)]
35. Teodorescu, R.; Liserre, M.; Rodríguez, P. *Grid Converters for Photovoltaic and Wind Power Systems*; Wiley: Chichester, UK, 2011.
36. Rocabert, J.; Luna, A.; Blaabjerg, F.; Rodríguez, P. Control of power converters in AC microgrids. *IEEE Trans. Power Electron.* **2012**, *27*, 4734–4749. [[CrossRef](#)]
37. Schroeder, D. *Electrical Drives—Control of Drive Systems (German: Elektrische Antriebe—Regelung Von Antriebssystemen)*, 4th ed.; Springer: Berlin, Germany, 2015.
38. Tripathi, S.M.; Tiwari, A.M.; Singh, D. Optimum design of proportional-integral controllers in grid integrated PMSG-based wind energy conversion system. *Int. Trans. Electr. Energy Syst.* **2016**, *26*, 1006–1031. [[CrossRef](#)]
39. Kaura, V.; Blasko, V. Operation of a phase locked loop system under distorted utility conditions. *IEEE Trans. Ind. Appl.* **1997**, *33*, 58–63. [[CrossRef](#)]
40. Vinayagam, A.; Swarna, K.S.V.; Khoo, S.Y.; Oo, A.T.; Stojcevski, A. PV based microgrid with grid-support grid-forming inverter control (simulation and analysis). *Smart Grid Renew. Energy* **2017**, *8*, 1–30. [[CrossRef](#)]
41. Gkoutaras, A. *Modeling Techniques and Control Strategies for Inverter Dominated Microgrids*. Ph.D. Thesis, Technical University of Berlin, Berlin, Germany, 2017.
42. De Brabandere, K. *Voltage and Frequency Droop Control in Low Voltage Grids by Distributed Generators with Inverter Front-End*. Ph.D. Thesis, University of Leuven, Leuven, Belgium, 2006.
43. SMA Solar Technology. Available online: <https://files.sma.de/dl/7418/lscpv-TI-en-17.pdf> (accessed on 18 January 2020).
44. Low, H. *Control of Grid Connected Active Converter*. Master’s Thesis, Norwegian University of Science and Technology, Trondheim, Norway, 2013.
45. *Verband der Elektrotechnik Elektronik Informationstechnik (VDE), VDE-AR-N 4105: Power Generating Plants in the Low Voltage Grid (German: Erzeugungsanlagen am Niederspannungsnetz—Technische Mindestanforderungen für Anschluss und Parallelbetrieb von Erzeugungsanlagen am Niederspannungsnetz)*; VDE Verlag GmbH: Berlin, Germany, 2018.
46. Blaschke, H. *Motor Protection (German: Motorschutz)*; VEB Verlag Technik: Berlin, Germany, 1954.
47. Ziegler, G. *Numerical Differential Protection: Principles and Applications*, 2nd ed.; Publicis: Erlangen, Germany, 2011.
48. Larsen & Turbo. Available online: <http://corpwebstorage.blob.core.windows.net/media/37784/omega-acb-catalogue.pdf> (accessed on 20 January 2020).
49. Eaton. Available online: [https://www.eaton.com/ecm/groups/public/@pub/@eaton/@holec/documents/content/ct\\_255776.pdf](https://www.eaton.com/ecm/groups/public/@pub/@eaton/@holec/documents/content/ct_255776.pdf) (accessed on 20 January 2020).
50. Meshcheryakov, V.P.; Sibatov, R.T.; Samoilo, V.V.; Topchii, A.S. Calculation of an interruption arc current and time of arc quenching in low-voltage current breakers. *Russ. Electr. Eng.* **2008**, *79*, 92–98. [[CrossRef](#)]
51. Maria, G.A.; Tang, C.; Kim, J. Hybrid transient stability analysis. *IEEE Trans. Power Syst.* **1990**, *9*, 384–391. [[CrossRef](#)]
52. Tang, C.K.; Graham, C.E.; El-Kady, M. Transient stability index from conventional time domain simulation. *IEEE Trans. Power Syst.* **1994**, *9*, 1524–1530. [[CrossRef](#)]
53. Mansour, Y.; Vaahedi, E.; Chang, A.Y.; Corns, B.R.; Garrett, B.W.; Demaree, K.; Athay, T.; Cheung, K. Hydro’s On-line transient stability assessment (TSA) model development, analysis and post-processing. *IEEE Trans. Power Syst.* **1995**, *10*, 241–253. [[CrossRef](#)]
54. Haque, M.H. Hybrid method of determining the transient stability margin of a power system. *IEE Proc. Gener. Transm. Distrib.* **1996**, *143*, 27–32. [[CrossRef](#)]
55. Zhang, Y.; Wehenkel, L.; Rousseaux, P.; Pavella, M. SIME: A hybrid approach to fast transient stability assessment and contingency selection. *Int. J. Electr. Power Energy Syst.* **1997**, *19*, 195–208. [[CrossRef](#)]

56. Kundur, P. *Power System Stability and Control*; McGraw-Hill: New York, NY, USA, 1994.
57. DgSILENT/PowerFactory. Available online: <https://www.digsilent.de/en/stability-analysis.html> (accessed on 22 January 2020).



© 2020 by the authors. Licensee MDPI, Basel, Switzerland. This article is an open access article distributed under the terms and conditions of the Creative Commons Attribution (CC BY) license (<http://creativecommons.org/licenses/by/4.0/>).